Embryo-derived brain-resident macrophages sustain sleep-wake circuits

Ali Seifinejad[1#*], Mojtaba Bandarabadi[2], Meriem Haddar[2],
Saskia Wundt[1], Anne Vassalli[2], Mehdi Tafti[2*], Gianni Monaco[1*]

[1] Institute of Neuropathology, Faculty of Medicine, University of Freiburg, Freiburg, Germany
[2] Department of Biomedical Sciences, University of Lausanne, Lausanne, Switzerland
#Present address: Department of Biomedical Sciences, University of Lausanne, Lausanne, Switzerland

[*]Correspondence to:
Dr. Ali Seifinejad: ali.seifinejad@mail.ch or
Prof. Mehdi Tafti: Mehdi.tafti@unil.ch or
Dr. Gianni Monaco: mongianni1@gmail.com

Summary

Sleep is a complex behavior regulated by a variety of brain cell types. The roles of brain-resident macrophages, such as microglia and CNS-associated macrophages (CAMs), including those derived postnatally, are not well defined. Here, we investigated the reciprocal interaction of brain-resident macrophages and sleep using multimodal high-throughput transcriptional, electrophysiological and metabolomic profiling in mice. We found that sleep deprivation caused profound transcriptional changes in microglia and CAMs, which were intensified by impaired sleep regulation in the absence of the important sleep-regulatory neuropeptide hypocretin/orexin (HCRT). Depletion in embryonically-derived brain macrophages caused increased sleep in the active period, but reduced its quality, reflected in reduced power of brain sleep oscillations. This was observed both for the Non-REM and REM sleep stages. Subsequent repopulation by postnatal brain macrophages unexpectedly failed to reestablish normal sleep-wake patterns and additionally induced sleep fragmentation. Furthermore, brain macrophage depletion caused excitatory-inhibitory synaptic imbalance, which was resistant to repopulation, and led to increased inhibitory synapses. At the metabolite level, the distinct metabolite profile induced by brain macrophage depletion largely returned to normal after repopulation. Our findings suggest a so far largely unknown interaction between brain-resident macrophages and sleep and emphasizes striking functional differences between embryonic and postnatally-derived brain macrophages, paving the way to future exploration of the role of brain macrophages of different origin in sleep disorders and synaptic connectivity.

Keywords: Microglia; CAM, vigilance states, sleep; HCRT

Introduction

Sleep is a complex behavior essential for the normal functioning of animals, consistently linked to various diseases when compromised(1). Sleep regulation involves circadian and homeostatic processes, determining respectively sleep timing and sleep need(2).

Sleep oscillatory patterns rely on the intricate connectivity of the central nervous system (CNS) at synaptic and neurotransmitter levels. Various cell types, primarily neuronal populations located in the hypothalamus, brainstem (BS), and basal forebrain (BF), interact to finely regulate sleep. The expression of synaptic proteins increases during wakefulness and sleep loss, and decreases during sleep(3), and the postsynaptic protein HOMER1A is a well-established core brain molecular correlate of sleep loss (4). Additionally, the release of key neuropeptides and neurotransmitters such as HCRT (also called Orexin), serotonin (5HT), noradrenaline (NA), and acetylcholine across different brain regions actively modulates sleep-wake cycles(5). This intricate interplay manifests in electroencephalographically (EEG) measurable readouts distinguishing wakefulness, non-rapid eye movement sleep (NREMS), and rapid eye movement sleep (REMS), characterized by distinct brain oscillatory activities such as delta waves (0.5-4 Hz) for NREMS and theta waves (6-9 Hz) for REMS in rodents. However, the contribution of non-neuronal cell types, such as brain-resident macrophages, to brain oscillations and sleep architecture remains largely unexplored.

Brain-resident macrophages comprising parenchymal microglia and CAMs(6-8), play significant roles in pathology and protecting the CNS from damage(9). Although the function of CAMs in regulating brain function is not well understood, microglia participate in a range of physiological functions including synaptic pruning(10). Microglial cells and leptomeningeal macrophages (as part of the CAMs) are derived from prenatal sources known as erythromyeloid precursors that engraft into the developing CNS(11, 12) and facilitate the establishment of neuronal networks especially in the first postnatal weeks (10). If embryonic microglial cells are depleted in adulthood, they repopulate from surviving endogenous cells (13). D*e novo* establishment of micoglial networks occurs by surviving cells through clonal

expansion (14) and these postnatal-derived microglial cells exhibit a different transcriptional signature (15). However, whether adulthood-derived microglia exhibit functional differences relative to orginal embryo-derived populations is largely unknown.

While a few studies have demonstrated a bidirectional relationship between embryo-derived microglia and sleep/wake states (16-19), a comprehensive understanding of how these two compartments modulate each other is still lacking. Specifically, the transcriptional signature of microglia and CAMs in response to sleep loss remains unknown. Conversely, the extent to which brain-resident macrophages impact sleep EEG activity requires thorough investigation through extensive EEG analysis. Moreover, the influence of brain macrophages on sleep-regulating neurotransmitters, neurochemical content, and synaptic connectivity warrants further exploration. Furthermore, it remains unclear whether adulthood-derived microglia are capable of re-establishing neural circuitries in the same manner as prenatal microglial cells, including synaptic plasticity and neurochemical balance, which are crucial for normal sleep regulation.

Here, we first studied the impact of sleep deprivation on the transcriptional signature of microglia and CAMs. Next, through in-depth analysis, we explored whether absence of embryo-derived microglia and CAMs influences sleep EEG patterns and whether repopulated postnatal microglia and CAMs can normalize these patterns. Finally, we investigated how the absence of microglia and CAMs affects brain network connectivity and neurochemistry.

Results

Sleep loss markedly alters the transcriptional profile of microglia and CAMs

We first investigated how lack of sleep impacts brain-resident macrophages. Sleep deprivation (SD) has shown to induce functional alterations in microglia(20, 21), however, its impact on the transcriptional profile of microglia and CAMs has not yet been documented. We thus deprived wild-type (WT) mice of sleep for 6 h (starting from light onset) and immediately afterward isolated microglia (CD11b^{+}, CD45^{intermediate}) and CAMs (CD11b^{+}, CD206^{+}, Fig. 1 A-B) from the cortex and hypothalamus, 2 major sleep-regulating centers, and performed gene expression analysis. The control group was not sleep deprived. We extracted RNA and performed bulk RNA sequencing (RNA-seq) to compare the transcriptome between SD and control conditions. After 6 hours SD, no changes were observed in expression of microglial core genes (*Hexb*, *P2ry12*, *Trem2*, and *TMEM119*) across the cortex and hypothalamus (Supplementary Fig. 1A). However, we observed many other differentially expressed genes (DEGs) (110 genes) (Figure 1C). While almost an equal number of genes were differentially regulated in cortex and hypothalamus after SD, we found genes only affected either in the cortex (e.g. *Cul1*, *Ints6l*, and *Ccnl2*) or the hypothalamus (e.g. *Slc1a3*, *Pdia3*, and *Rpn1*) (Supplementary Fig. 2) indicating region-specific microglial response to SD. Gene set enrichment analysis of the DEGs in WT mice revealed an enrichment of pathways related to protein folding, such as ‘Positive regulation of protein folding’ (Fig. 1D).

We next investigated how SD affects the transcriptome of CAMs. As CAMs are not abundant in the brain, we sorted them from the entire brain. Our results revealed that 6 h of SD induced numerous DEGs in CAMs (Fig. 1E). Among them, both the *App* and *Lyve1* genes (Fig. 1F) were previously linked to Alzheimer's disease (AD) pathogenesis (22, 23). Remarkably, *Lyve1* gene expression almost tripled after 6 h of SD. Gene set enrichment analysis of DEGs of CAMs in WT mice revealed enrichment for pathways related to AD, including ‘Positive regulation of tau-protein kinase activity’ (Fig. 1G).

To further understand the effect of sleep on brain-resident macrophages, we additionally, analyzed the transcriptome of microglia and CAM in mice with a disrupted regulation of sleep,

123 the *Hcrt-ataxin-3* transgenic mice (hereafter referred to as Ox-Ataxin mice), which experience
124 HCRT neuronal degeneration during development (24). HCRT neurons play a critical role in
125 waking behaviors that drive sleep need (25). Ox-Ataxin mice represent a model for narcolepsy
126 disease, manifesting excessive daytime sleepiness, fragmentation of wake and sleep.
127 Transcriptional comparison of SD and control conditions in microglia of OX-Ataxin mice
128 resulted in a larger number of DEGs compared to WT mice (270 vs 110 genes) (Figure 1H, I),
129 suggesting that sleep loss significantly increases the transcriptional change in microglia in the
130 mice with disrupted sleep regulatory pathways. Among the DEGs, some were shared between
131 the two mouse lines, however, Ox-Ataxin mice exhibited many DEGs that were not
132 differentially regulated in WT mice in response to sleep loss (e.g. *Naglu*, *Lyz2*, *Rsp9*, *Rps29*,
133 *Stip1*) (Fig. I). We additionally found that SD primarily affects cortical, rather than hypothalamic
134 microglia in Ox-Ataxin mice, indicating that the cortical microglia are more susceptible to
135 vigilance state instability induced by the lack of wake-promoting neuropeptide HCRT
136 (Supplementary Fig. 2). While we did not detect the expression of HCRT receptors in
137 microglia, we observed the expression of downstream circuit receptors, including
138 noradrenaline and serotonin receptors, in microglia. One such gene is the beta-2 adrenergic
139 receptor (*Adrb2*), which is predominantly expressed in hypothalamic microglia compared to
140 cortical microglia (Supplementary Fig. 1B). Gene set enrichment analysis of the DEGs in
141 microglia of Ox-Ataxin mice revealed an enrichment of pathways like "Virion attachment to
142 host cell" (Fig. 1J).
143 Overall, in the two mouse lines, we found microglial genes primarily regulated under the SD
144 condition, such as *Cirbp*, *Ighd*, and *Npnt* (Fig. 1K). Additionally, we found genes that were
145 more expressed in the hypothalamus compared to the cortex (Fig. 1L). Furthermore, we
146 observed that genes such as *Sgk1* and *Pecr* were largely regulated after SD in the
147 hypothalamus but not in the cortex, suggesting structure-specific microglia changes after SD
148 (Fig. 1M). Lastly, we found genes that were exclusively regulated in Ox-Ataxin mice such as
149 *Slc31a2*, *Lyz2*, and *Ccl4* (Fig. 1N).

150 Analysis of SD vs control conditions in CAMs of Ox-Ataxin mice surprisingly revealed a
151 profoundly diminished number of DEGs relative to WT mice (only 6 genes), suggesting that
152 CAMs show a blunted response to sleep deprivation in absence of a functional HCRT system
153 (Fig. 1O).
154 In summary, our data show that sleep significantly influences the transcriptional profiles of
155 brain-resident macrophages, indicating intricate interactions between these two systems. SD
156 induces major changes in the transcriptional profile of microglia and CAM genes involved in
157 disease-related pathways.
158
159 **Repopulated adulthood-derived microglia are deficient in rebuilding normal NREMS**
160 **circuitry**
161 We next examined to what extent embryo-derived brain-resident macrophages contribute to
162 sleep regulation and whether postnatal-derived macrophages can perform the same function.
163 To address this, we depleted microglia from the brains of mice for two weeks using colony-
164 stimulating factor 1 receptor (CSF1R) inhibition via PLX5622 (26), and then allowed them to
165 repopulate for four weeks (Fig. 2A). CSF1 receptor is vital for microglia survival. Antagonizing
166 it severely depletes microglia within three days, and upon the termination of treatment,
167 repopulation can be readily observed within a few days(15). We observed substantial microglia
168 depletion (>86%) after two weeks of PLX5622 treatment, and complete repopulation four
169 weeks after withdrawal (Fig. 2B, C).
170 We recorded EEG signals before depletion (control), after depletion and after repopulation
171 (Fig. 2A). Since CSF1 inhibition also depletes CAMs(27), the effects we report here are due
172 to the depletion of both cell types, which we refer to collectively as MG. Our experimental
173 conditions therefore included control, MG-Dep (microglia/CAM depleted), and MG-Repop
174 (microglia/CAM repopulation). To evaluate the distribution of vigilance states, we employed
175 our standard sleep/wake phenotyping protocol(28), with two days of baseline (which were
176 averaged and presented as one day in the figures) and in the third day mice underwent 6 h of
177 SD (ZT0-ZT6) and 18 h of recovery (Fig. 2D). In baseline conditions, all experimental mice

178 demonstrated the characteristic cycling behavior, with higher levels of wakefulness during the
179 dark period and higher levels of NREMS during the light period and exhibited the increase in
180 NREMS amounts in response to SD (Fig. 2E, F). However, a significant NREMS increase was
181 observed in the baseline dark period when comparing the MG-Dep to the control condition.
182 Interestingly, the repopulation of MG did not normalize this effect (Control: 12.75±0.72 min,
183 MG-Dep: 16.78±0.77 min, MG-Repop: 16.54±0.70 min, mean ± SEM) (Fig. 2E, F, bottom
184 panels). Reciprocally, there was a notable reduction in wakefulness during the dark period
185 (Fig. 2E, F, top panels).
186 To gain insight into sleep homeostatic regulation in different mouse groups and determine
187 whether increased sleep is due to increased need for sleep, we analyzed the time course of
188 NREMS EEG delta power (1-4 Hz, a recognized quantitative readout of sleep need) across
189 our 3-day recordings. All mice groups showed a typical decline in delta power during the light
190 period and a strong rebound after SD, indicating homeostatic regulation of sleep need in all
191 groups (Fig. 2G). However, the buildup in delta power during the baseline dark period was
192 significantly lower in MG-Dep and MG-Repop mice compared to WT mice (Fig. 2G). This
193 attenuation was more pronounced in MG-Repop mice and may be partly related to the
194 increased amount of sleep during the baseline dark period (Fig. 2E, lower panel). In contrast,
195 when mice were exposed to enforced wakefulness (SD), the EEG delta power increase was
196 significantly more pronounced in MG-Dep and MG-Repop than in control conditions, and again
197 this effect was more extensive in MG-Repop than in MG-Dep (Fig. 2G). Altogether, these data
198 indicate impaired buildup of homeostatic sleep need during the waking period.
199 Spectral analysis of NREMS revealed that MG-Dep mice exhibited higher slow-delta (1-2 Hz)
200 activity compared to control mice in baseline light period (Fig. 2H, left). This frequency band
201 appears particularly affected also in MG-Repop mice, as it was significantly increased in the
202 recovery light period following SD (Fig. 2I, left). The fast-delta (3-4 Hz) frequency range was
203 in contrast blunted during both baseline and recovery light periods only in the MG-Dep
204 condition (Fig. 2H, I, left). During the baseline dark period, large delta power blunting was
205 observed in both MG-Repop (1.5-3.5 Hz) and MG-Dep (3-5.5 Hz) conditions. These deficits

206 remained nearly the same during the recovery dark period, indicating that NREMS of both
207 experimental mice appears to be shallower (Fig. 2H, I, right). Collectively, it can be concluded
208 that the presence of MG is necessary for the precise regulation of fast and slow-delta power
209 as a proxy of the sleep homeostatic process. MG repopulation not only fails to restore NREMS
210 regulation but worsens it.
211 To determine whether increased NREMS duration is due to enhanced state initiation
212 (increased number of NREMS episodes) and/or to enhanced state maintenance (increased
213 NREMS episode duration), we conducted a sleep fragmentation analysis. We found that while
214 MG-Dep mice have similar sleep bout duration patterns as the control condition, MG-Repop
215 mice showed a larger number of shorter NREMS bouts (16 seconds [Control: 6.7±0.63, MG-
216 Dep: 6.8±0.7, MG-Repop: 9.84±1.12]) and 64 seconds [Control: 12.12±1.15, MG-Dep:
217 11.02±0.81, MG-Repop: 17.63±1.2]) and fewer longer NREMS bouts (>256 seconds [Control:
218 1.96±0.28, MG-Dep: 1.74±0.33, MG-Repop: 0.62±0.17]), suggesting a strong destabilization
219 of NREMS in the MG-Repop brain (Fig. 2J).
220 During NREMS, brief bursts of brain activity in the 9-16 Hz frequency range, called spindles,
221 are generated by thalamo-cortical interactions and play roles in processes such as learning,
222 memory, and cognition(29). To determine if MG depletion and repopulation influence spindle
223 generation, we quantified spindle rate during NREMS episodes and found a significantly
224 reduced spindle rate in MG-Dep mice compared to the control condition (Fig. 2K, L; see
225 “Methods”). In contrast to other features of NREMS, MG repopulation was found to normalize
226 the occurrence rate of spindle events, indicating that MG repopulation partially rescues the
227 circuit deficits seen after MG depletion.
228 Altogether, these data suggest that embryo-derived MG are an integral part of NREMS
229 establishment and maintenance, and repopulated postnatal MG largely fail to fulfill the normal
230 NREMS regulatory functions of embryo-derived MG.
231
232 **Depletion of microglia prolongs REMS and degrades its quality**

233 Different neural pathways and neurotransmitters regulate REMS compared to NREMS.
234 However, the role of MG in the regulation of REMS is not well understood. We quantified
235 REMS amount across the dark/light periods and found that MG-Dep mice display more REMS
236 compared to the control and MG-Repop conditions during the baseline dark period (Control:
237 0.67±0.1, MG-Dep: 1.17±0.21 min/h, mean ± SEM). However, in contrast to NREMS, MG
238 repopulation corrected the abnormal expression of REMS (MG-Repop: 0.61±0.13 min/h) (Fig.
239 3A, B). To investigate if the increase in REMS is due to the consolidation of this state, we
240 performed fragmentation analysis and found that the number of shorter REMS bouts (8 s) is
241 largely decreased (Control: 8.7±2.05, MG-Dep: 2.8±1.2, MG-Repop: 8.8±3.3) and longer
242 bouts (>2 min) are increased (Control: 1.5±0.8, MG-Dep: 6.1±1.1, MG-Repop: 4.71±1.4, mean
243 ± SEM) (Fig. 3C) in MG-Dep mice, suggesting stabilization of REMS in the absence of MG.
244 Theta oscillations dominate the EEG signal during REMS, where theta phase dynamically
245 modulates gamma amplitude in hippocampal and cortical networks(30). We next investigated
246 the contribution of MG in theta oscillations and theta-gamma interactions. Spectral analysis of
247 REMS revealed a significant dampening of theta (6-8 Hz) power in MG-Dep mice during the
248 baseline dark period (Fig. 3D), which was restored after MG repopulation. We also found that
249 the theta-gamma coupling is significantly reduced in the MG-Dep condition compared to the
250 control. Although MG repopulation attempts to bring it back to the normal level, it fails
251 significantly (Fig. 3E, F).
252 Altogether, these findings suggest that the presence of MG is necessary for the normal
253 expression of REMS.
254
255 **Microglia contribute to the maintenance of active wakefulness**
256 The quality of prior wakefulness contributes to the expression of both NREMS and REMS.
257 Along these lines, a specific sub-state of prior wakefulness was recently proposed to drive
258 NREMS need (25), and some aspects of wakefulness may functionally substitute for REMS
259 (31). To investigate how wakefulness is expressed in our experimental conditions, we
260 performed a dynamic analysis of the full waking EEG spectrum across three recording days.

261 This global analysis revealed differential expression of the higher waking frequency bands
262 during light-dark cycles across three days, and most notably during enforced wakefulness
263 (SD). As suggested in Figure 4 (Fig. 4A), both MG-Dep and MG-Repop mice exhibit a large
264 dampening of the lower gamma (≈45-55 Hz) band during the baseline dark period, which is
265 exacerbated during the recovery dark period. Additionally, the MG-Dep mice exhibit a large
266 blunting of the higher gamma band (≈70-90 Hz) during SD, which partially normalizes after
267 MG repopulation. To better quantify the lower frequency bands, we performed PSD analysis
268 and found that MG-Dep mice exhibit a large increase in slow delta (1.35-1.75 Hz) activity
269 compared to the control mice (Fig. 4B).
270 Mice spend a portion of their waking time engaged in exploratory and motivated behaviors,
271 such as running, nest building, or drinking, often referred to in rodents as "active wakefulness".
272 These behaviors are associated with the EEG signature called "theta-dominated wakefulness"
273 (TDW 6.0-9.5 Hz), which has been suggested to be the principal driver of the sleep homeostat
274 (25). We quantified TDW in our mice and found a large decrease in its amount in both MG-
275 Dep and MG-Repop mice during the baseline dark period (Fig. 4C, D). This reduction was
276 more pronounced in MG-Repop mice, which was also seen during SD (Fig. 3C, E). TDW is
277 associated with heightened gamma activity. We analyzed the time course of gamma activity
278 during wakefulness and found an increase in slow (32-45Hz) frequency bands in the MG-
279 Repop condition compared to the controls (Fig. 4F). The increase in these frequency bands
280 in MG-Repop mice is also apparent on time-frequency heat maps in Figure 4A.
281 Overall, these data suggest a significant imbalance in the theta/gamma-rich waking state in
282 both the MG-Dep and MG-Repop conditions, and appearance of heightened gamma activity
283 after MG repopulation.
284
285 **Disrupted balance of synaptic signaling upon microglial depletion and repopulation**
286 Sleep is associated with changes in synaptic plasticity(32) and microglia play a substantial
287 role in synaptic functions, which are dependent on neuronal activity and vigilance states
288 (VS)(33). To investigate whether MG depletion and repopulation induce changes in brain

289 network connectivity at the synaptic level, we analyzed a subset of excitatory and inhibitory
290 synaptic density proteins that are involved in sleep regulation, (e.g., the core brain molecular
291 correlate of sleep loss, HOMER1) in the brains of our experimental mice.
292 Using an ImageJ macro, we counted the number of synapses on cortical and hypothalamic
293 neurons (Fig. 5A, B) and found that the number of excitatory VGLUT1-HOMER1 synapses on
294 $NEUN^+$ cortical neurons was significantly reduced in both MG-Dep and MG-Repop conditions.
295 This reduction was more noticeable in MG-Repop mice (Fig. 5C). Interestingly, this effect was
296 regulated at the postsynaptic level (HOMER1-associated, Fig. 5D) rather than the presynaptic
297 level (VGLUT1-associated, Fig. 5E). Recently, cortical PV neurons have been proposed to be
298 responsible for homeostatic sleep regulation(34). We found that the number of parvalbumin
299 (PV)-originated(35) Synaptotagmin-2-Gephyrin (Syt2-Geph) inhibitory synapses on the
300 cortical $NEUN^+$ neurons was significantly increased under the MG-Repop condition (Fig. 5F,
301 G). This increase could possibly be due to an increase in the activity of PV neurons, as we
302 found that the number of VGLUT1-HOMER1 excitatory synapses on PV neurons was
303 significantly increased under both MG-Dep and MG-Repop conditions (Fig. 5H, I). We
304 additionally investigated the changes in the count of VGLUT1-HOMER1 synapses on
305 representative hypothalamic neurons (HCRT) and found a significant decrease in the number
306 of VGLUT1-HOMER1 synapses on HCRT neurons in both MG-Dep and MG-Repop conditions
307 (Fig. 5J, K).
308 To further investigate changes in network connectivity in the brains of MG-Dep and MG-Repop
309 mice, we analyzed additional synaptic markers and sleep-specific neurotransmitter receptors
310 (e.g., receptors of monoaminergic systems and neuropeptides) on RNA extracted from cortical
311 samples of these mice. Our bulk analysis revealed that some general synaptic markers, such
312 as *Synaptophysin I* (*Syp*), are largely downregulated in both experimental mice, while *Slc17a7*
313 (encoding Vesicular glutamate transporter 1) and *Homer1* genes are significantly
314 downregulated in the cortex of the MG-Repop condition. Among the specific neurotransmitter
315 markers analyzed, the adrenergic receptor family (e.g. *Adrb2*, *Adra2a*, *Adrb3*, and *Adra1a*)
316 genes showed a tendency to be less expressed in both MG-Dep and MG-Repop conditions,

317 with a marked decrease in the expression of the *Adra2a* gene. Additionally, we observed a
318 reduction in expression of *Cholinergic receptor muscarinic 2* (*Chrm2*) and the serotonergic
319 receptor *5-Hydroxytryptamine receptor 1A* (*Htr1a*) genes, which mainly occur in the brain of
320 MG-Repop mice (Fig. 5L).
321 Taken together, these data suggest that brain connectivity at the synaptic level is largely
322 impaired following the depletion of brain-resident macrophages. Repopulating the brain with
323 these macrophages not only failed to normalize connectivity but, in many cases analyzed,
324 worsened it.
325
326 **Neurotransmitter release is largely restored after the repopulation of resident**
327 **macrophages**
328 Synapses, in addition to providing structural connections in the brain, play a crucial role in
329 transmitting neurotransmitters essential for the function of complex neural systems. We
330 therefore questioned whether the levels of essential neurotransmitters involved in sleep
331 regulation are affected by the depletion and repopulation of brain-resident macrophages. We
332 conducted targeted metabolomics to analyze the neurotransmitter content and metabolite
333 reservoir of the cortex, target of most neurotransmitters and region where EEG signals are
334 acquired. Assessment of neurotransmitter content was performed using chromatography with
335 tandem mass spectrometry (LC-MS/MS) in the brain of control, as well as MG-Dep and MG-
336 Repop mice. We found that pharmacological depletion of MG led to a distinct clustering of
337 metabolites, as indicated by principal component analysis (PCA) (Fig. 6A). This suggests that
338 MG plays an important role in maintaining the overall metabolic composition of the cortex. MG
339 repopulation however restored the cortical submetabolome to a pattern similar to the one
340 observed under control experimental conditions (Figure 6A). Univariate analysis revealed a
341 reduction in norepinephrine upon MG depletion, which was restored after repopulation (Figure
342 6B). The concentrations of acetylcholine, choline, dopamine, and serotonin remained
343 unchanged between the experimental conditions, with a slight tendency to decrease in MG-
344 Dep condition.

345 Furthermore, we observed that MG depletion led to a marked reduction of L-2-amino adipic
346 acid (L-2-AAA), which was only partially recovered after repopulation (Figure 6B). We also
347 analyzed the precursors of neurotransmitters and found a significant decrease in the amino
348 acids L-serine and asparagine under depleted condition, which could be restored upon MG
349 repopulation (Figure 6C). Similarly, there was a trend towards decreased glycine and L-
350 glutamic acid content (Figure 6C).
351 Taken together, our data suggest that while network connectivity is significantly impaired in
352 MG-Dep condition and resistant to MG repopulation, the underlying substrates
353 (neurotransmitters and metabolites) are largely restored after MG repopulation.
354

355 **Discussion**

356 In this study, we investigated the reciprocal interaction between sleep and brain-resident
357 macrophages. We first analyzed the transcriptional changes in microglia and CAMs in
358 response to sleep loss. While the effects of sleep on oligodendrocytes(36) and astrocytes(37)
359 have been documented, its effects on brain-resident macrophages are less explored. We
360 show that lack of sleep induces significant transcriptional changes in both MG and CAMs,
361 These changes are further amplified when the normal sleep-regulatory system is impaired, as
362 seen in the narcolepsy OX-Ataxin mouse model. We found that the altered genes are involved
363 in disease-related pathways including regulation of protein folding and Tau-protein kinase
364 activity. These pathways are involved in neurodegeneration(38, 39), and the role of microglia
365 in sleep loss-associated neurodegeneration is under investigation(17, 40). Our data showed
366 that removing the important sleep-regulating neuropeptide, HCRT, induces massive
367 transcriptional changes in both microglia (increased number of DEGs) and CAMs (decreased
368 number of DEGs). Previous studies have shown that a null mutation in the *Hcrt* gene in an AD
369 mouse model leads to a significant reduction in Aβ brain pathology(41), and human narcolepsy
370 patients who lack a functional HCRT system display reduced amyloid burden(42). It can be
371 speculated that this effect is mediated by either microglia or CAMs. Further investigations are

372 warranted to decipher these interactions. We additionally found region-specific transcriptional
373 response to sleep loss in microglia highlighting that local microglia differentially participate in
374 neural functioning of the brain as previously suggested(43, 44).
375 In a reciprocal analysis, we also investigated whether embryo-derived MG contribute to sleep
376 regulation, and whether postnatal-derived MG serve a similar role. We demonstrate that MG
377 depletion has a significant impact on the homeostatic regulation of sleep. The brain circuits
378 most vulnerable to microglia depletion and repopulation, causing the changes in sleep EEG
379 that we document, are still unknown. However, changes in slow-delta activity in NREM sleep,
380 state stabilization and reduced theta power in REMS, as well as changes in waking slow-delta
381 activity, were reported in mice with defects in hypothalamic HCRT and brainstem serotonergic
382 and noradrenergic systems(25, 28, 45, 46). This is suggestive of functionally important local
383 interactions between microglial populations and sleep regulating circuits, as mentioned above.
384 We showed that the changes in sleep patterns after MG depletion are not fully reversed after
385 MG repopulation. Previous studies have shown that the brain global transcriptomes are little
386 influenced by repopulated microglia(15). Furthermore, it has been suggested that after MG
387 repopulation, neuroprotection is achieved through IL-6 induction by neurons(47). Other
388 studies reported full functionality of retinal microglia after repopulation, including continuous
389 retinal surveillance, maintenance of synaptic structure, and normal behavioral and
390 physiological responses to retinal injury (48). However, our data reveal that MG repopulation
391 not only fails to completely restore various aspects of sleep regulation, but in some cases
392 exacerbates altered parameters, such as fragmentation of NREMS and dysregulation of sleep
393 need. This demonstrates striking funtional differences between microgial cells derived from
394 pre-or postantal sources. We speculate that not all microglia-neuronal interactions are
395 properly reestablished by adulthood-derived microglia after repopulation. Whether a longer
396 repopulation period might correct the abnormalities observed in our analysis warrants further
397 investigation. We observed a significant imbalance between excitatory and inhibitory
398 synapses after depletion of embryo-derived microglia and after repopulation with adult
399 microglia, with a notable increase in inhibitory synapses following repopulation. Studies in

juvenile mice prevously reported that microglia depletion in the developing brain significantly increases the number of both excitatory (VGLUT1-HOMER1) and inhibitory (Syt2-Gephyrin) synapses on cortical neurons, an effect that persisted after repopulation until P30. However, in the adult (P60) brain, synapse density returned to normal control levels, suggesting that depleting microglia during development causes long-lasting, albeit not permanent, effects(49). Our data, however, show that depleting microglia in adulthood, and then repopulating them, induces different results, with a reduction in excitatory synapses in both MG-Dep and MG-Repop conditions, and an increase in inhibitory synapses in MG-Repop conditions. In the developing brain, it has been suggested that MG-Dep impairs synaptic pruning processes and alters related gene expression(10, 49). Whether the same process or any specific pathways are induced by MG depletion and repopulation in the adult brain, such as aberrant reactivation of developmental programs(50), remains to be found.

Furthermore,other studies have suggested that microglia play a role in restraining excessive neuronal activation that cannot be sufficiently suppressed by inhibitory neurons alone(51). Our results suggest that embryo-derived microglia also control excessive activity of inhibitory PV neurons, but the reasons why this is not corrected with adulthood-derived microglia remain to be investigated.

Deficient synaptic neurotransmission was proposed as a potential cause for abnormal sleep regulation(52). We found here an imbalanced neurotransmitter and metabolite content of the brain in mice devoid of prenatal microglia. It appears that norepinephrine neurotransmission is particularly sensitive to MG deficiency, as both the levels of norepinephrine metabolites and the corresponding receptors are significantly affected by MG depletion. Norepinephrine is implicated in both wakefulness(53) and sleep regulation(54-56), and it has been suggested that microglial surveillance process relies heavily on norepinephrine signaling(57, 58). Additionally, we observed a decrease in the expression of neurotransmitter precursors such as L-serine, which was mirrored by changes in the concentrations of glycine, asparagine, and glutamic acid. Previous studies have proposed serine as a link between metabolism and

427 neurotransmission (59), and serine serves as a precursor for synthesizing ceramide (60),
428 which has been suggested to be essential for maintaining stable wakefulness (61).
429 Our findings indicate that MG affect vigilane state regulation via multiple pathways and play
430 a more substantial role in maintaining the physical connectivity of brain networks rather than
431 neurochemical connectivity, as MG repopulation largely restores metabolites but not
432 synapses. To gain a detailed understanding of MG regulation of sleep, it will be necessary to
433 explore local specific microglial depletion, and disruption of microglia-neuron interactions
434 using inducible systems. Additionally, investigating the separate contributions of microglia and
435 CAMs in sleep regulation using Cre lines under the promoter of *Hexb* (62) and *Mrc1* (63)
436 genes, respectively, would be a starting point. The observed vigilance state phenotypic
437 alterations may also be influenced by disruptions in central factors (such as protein
438 phosphorylation orchestrated by microglial TNF-α)(16), and peripheral players (since CSF1R
439 inhibition also effects circulating and tissue macrophages)(64) warranting further
440 investigations. Overall, our results shed new light on the complex interaction between the
441 neuroimmune system and sleep regulation, and it paves the way for future investigations in
442 this important physiopathological field.
443

444 **Data availability**

445 All data are available from the corresponding author upon reasonable request. Bulk RNA
446 sequencing datasets were deposited into the Gene Expression Omnibus database under
447 accession number XXXXX and are available at the following URL: XXXXXXXX.

448 **Acknowledgements**

449 We extend our gratitude to the Metabolomics Core Facility at the Department of General
450 Pediatrics, University of Freiburg, with special thanks to Dr. Luciana Hannibal and Victoria
451 Wingert for their invaluable support and expertise. AS was supported by Novartis Foundation
452 for medical-biological Research (#23B079). MB was supported by the Swiss National Science

453 Foundation (grant 190605). MT was supported by Swiss NSF (grant 201235), and the State
454 of Vaud (Faculty of Biology and Medicine, University of Lausanne). AV was supported by the
455 Swiss National Science Foundation (grant 31003A_182613).

456 **Author contributions**

457 AS conceptualized and designed the study. AS, MH, and SW performed experiments. AS,
458 GM, and MB analyzed data. AS, GM, AV, MT, and MB wrote the manuscript.
459
460
461 **Declaration of interests**

462 The authors declare no competing interests.
463

464 **Methods**

465 **Animals.** Wild type (C57BL/6J) and Ox-ataxin-3 transgenic mice were used in this study. All animals
466 were between 12 and 14 weeks old during the time of experiments and animal experiments were
467 approved by the Ministry for Nature, Environment and Consumers` Protection of the state of Baden-
468 Württemberg and were performed in accordance to the respective national, federal, and institutional
469 regulations. At all times, care was taken to minimize animal discomfort and avoid pain.
470

471 **Microglia and CAM isolation and flow cytometry.** Mice brains were collected and microglia were
472 enriched using density gradient separation and were prepared as described previously (65, 66). The
473 cell suspension was then incubated with Fixable Viability Dye eFluor® 780 (1:1000, 65-0865-14,
474 Invitrogen) for 10 min at 4 °C. Subsequently, the following antibodies were used: antiCD11b (1:200,
475 clone M1/70, 101235 Biolegend), anti-CD45 (1:200, clone 30-F11, 103108 BioLegend), anti-CD11c
476 (1:100, 12-0114-81, Invitrogen), anti-Gr1 (1:200, 108408, Biolegend) and anti-CD206 (1:200, 141708,
477 Biolegend). Cell sorting for RNA-seq was performed on a MoFlo Astrios (Beckman Coulter).
478

479 **Total RNA extraction.** Total RNA was extracted from FACS sorted mouse brain cells stabilized in
480 RNAprotect buffer according to the "Purification of total RNA from animal and human cells" protocol of
481 the RNeasy Plus Micro Kit (QIAGEN, Hilden, Germany).
482 In brief, cells were stored and shipped in buffer RNAprotect at 2-8 °C. After pelleting by centrifugation
483 for 5 minutes at 5,000 x g, the RNAprotect was replaced by 350 µl buffer RLT Plus and the samples
484 were homogenized by vortexing for 30 seconds. Genomic DNA contamination was removed by using
485 gDNA Eliminator spin columns. Next one volume of 70 % ethanol was added and the samples were

applied to RNeasy MinElute spin columns followed by several wash steps. Finally the total RNA was eluted in 12 µl of nuclease free water. Purity and integrity of the RNA was assessed on the Agilent 2100 Bioanalyzer with the RNA 6000 Pico LabChip reagent set (Agilent, Palo Alto, CA, USA).

RNA sequencing. The SMARTer Ultra Low Input RNA Kit for Sequencing v4 (Clontech Laboratories, Inc., Mountain View, CA, USA) was used to generate first strand cDNA from approximately 1 ng total-RNA. Double stranded cDNA was amplified by LD PCR (13 cycles) and purified via magnetic bead clean-up. Library preparation was carried out as described in the Illumina Nextera XT Sample Preparation Guide (Illumina, Inc., San Diego, CA, USA). Thereby 150 pg of input cDNA were tagmented (tagged and fragmented) by the Nextera XT transposome. The products were purified and amplified via a limited-cycle PCR program to generate multiplexed sequencing libraries. For the PCR step 1:5 dilutions of the unique dual indexing (i7 and I5) adapters were used. The libraries were quantified using the KAPA Library Quantification Kit - Illumina/ABI Prism User Guide (Roche Sequencing Solutions, Inc., Pleasanton, CA, USA). Equimolar amounts of each library were sequenced on an Illumina NextSeq 2000 instrument controlled by the NextSeq 2000 Control Software (NCS) v1.4.0.39521, using one 50 cycles P3 Flow Cell with the dual index, single-read (SR) run parameters. Image analysis and base calling were done by the Real Time Analysis Software (RTA) v3.9.2. The resulting .cbcl files were converted into .fastq files with the bcl2fastq v2.20 software. RNA extraction, library preparation and RNAseq were performed at the Genomics Core Facility "KFB - Center of Excellence for Fluorescent Bioanalytics" (University of Regensburg, Regensburg, Germany; www.kfb-regensburg.de). Bulk RNA-seq data was aligned with STAR v2.7.10a (67) to the mouse reference genome Gencode M26 (68). Counts were obtained from the bam files with the tool featureCounts v2.0.3. Genes with count expression higher than 5 in at least 3 samples were kept for the differential expression analysis. Differential expression was performed using the limma trend method (69) on the log2 counts per million (CPM) values. Venn diagrams and Volcano plots were generated with the R packages limma and EnhancedVolcano, respectively. Enrichment analysis was performed using ShinyGO (70).

Gene expression analysis. For qPCR analysis, RNA extracted from the cortical samples of control, MG-Dep and MG-Repop mice. RNA was extracted using RNeasy micro kit (74004) and cDNA synthesis was performed using random hexamer primers and M-MLV Reverse Transcriptase Promega kit (M3682). SYBR green-based and Taqman probes were used to detect the gene expression. The assay was performed using a LightCycler480 (Roche).

Immunofluorescence and synapse counting. Mice were anesthetized with ketamine (100 mg per kg body weight) and xylazine (10 mg per kg body weight) followed by perfusion with 1× PBS. For histology, brains were kept overnight in 4% paraformaldehyde (PFA). Brains were then dehydrated in 30% sucrose for about 48 hours and then snap-frozen on dry ice. Cryosections (14µm for synapse counting and 20µm for microglia and CAM staining) from brain tissue were prepared as free floating in PBS. The following antibodies were used to stain microglia, CAM and synapses: Rabbit-anti-IBA1 (ab178846, abcam), Rat-anti-CD206 (Biorad MCA2235), Goat-anti-Collagen type 4 (Millipore AB769), anti-NEUN

526 (ab177487, ab104224, abcam), anti-VLUT1 (135304, synaptic system), anti-HOMER1 (ABN37,
527 Millipore), anti-Gephyrin (147318, synaptic system), anti-Synaptotagmin-2 (ZDB-ATB-081002-25,
528 ZFIN), anti-Parvalbumin (MAB1572, Merck) and anti-HCRT-A (SC-8070). The DAPI was used to stain
529 the nucleus. Rat-anti-CD206 and Goat-anti-Collagen type 4 antibodies were incubated for 48 hours at
530 4 °C to have high quality staining. Iba1 antibody was incubated overnight at 4 °C and the primary
531 antibodies to detect synapses were incubated for 1.45hr at room temperature. The brain cuts were
532 incubated with secondary antibodies for 1-2 hours at room temperature. Fluorescence imaging was
533 performed with TCS SP8 X (Leica Microsystems). Imaging of synapses was performed using 63X
534 objective with zoom factor 8. Iba1^{+} cells were counted using Fiji. Synapse analysis and quantification
535 were conducted using Fiji macro developed previously (71) with little modifications.
536
537 **Quantitative profiling of metabolites by liquid chromatography and mass spectrometry (LC-**
538 **MS/MS).** Mice brain tissue biopsies were thawed and homogenised with ice-cold PBS supplemented
539 with 1% protease inhibitor cocktail (Sigma Nr. P8340-5ML), using a cordless pestle motor and
540 disposable pellet mixers (VWR Nr. 47747-366). Buffer volume was adjusted to reach a target of 0.1 to
541 0.3 mg wet-tissue/mL lysis buffer. Whole tissue homogenates were aliquoted for downstream
542 measurement of total protein concentration, flash-frozen and stored at -80 °C. Sulfur-containing
543 metabolites as well as creatinine, S-adenosylmethionine and S-adenosylhomocysteine were
544 determined according to a previously published procedure (72, 73). Lactate, TCA and glycolysis
545 intermediates and other organic acids, and folates were determined as described in previous work (74).
546 Amino acids and neurotransmitters were determined using a previously described protocol (75, 76). A
547 commercially available standardized amino acid mixture was utilized to generate a calibration curve for
548 amino acids (Amino acid standards, physiological, Sigma, Nr. A9906-10ML). Calibration curves for all
549 other metabolites were prepared from individual stock solutions prepared in house. Quantitation
550 accuracy was examined by monitoring homocysteine and methylmalonic acid concentrations in an
551 external quality control, namely, the Control Special Assays in Serum, European Research Network for
552 the evaluation and improvement of screening, diagnosis, and treatment of Inherited disorders of
553 Metabolism (ERNDIM) IQCS, SAS-02.1 and SAS-02.2 from MCA Laboratories, Winterswijk,
554 Netherlands. For all other metabolites, quantitation trueness was tested by examining metabolite
555 concentrations in plasma from a previously validated sample isolated from a healthy control individual
556 with respect to standard reference ranges, using the same calibration curves and LC-MS/MS running
557 conditions. Quantification of metabolites was carried out with Analyst® 1.7.2 software, 2022 AB Sciex.
558
559 **Treatments.** In order to eliminate cells dependent on CSF1R (MG) mice were administered a CSF1R
560 inhibitor called PLX5622 (Plexxikon). The inhibitor was combined with AIN-76A standard chow at a
561 concentration of 1,200ppm (Research Diets) and the mice were given unrestricted access to it for two
562 weeks. The control group received AIN-76A standard chow without any modifications. After two weeks
563 the PLX5622 food was replaced with control food to start repopulation of MG.
564

565 **Mice surgery, data acquisition and vigilance state analysis.** Mice surgery and data acquisition were
566 performed as previously described (28). MATLAB scripts were created to quantify various parameters
567 related to wakefulness, NREMS and REMS. These parameters include time distribution and amount of
568 episodes, as well as the fragmentation of vigilance states, all of which were defined based on previously
569 established criteria (28). TDW analysis was conducted following the method described by Vassalli and
570 Franken (25).
571
572 **Power spectral analysis.** Using Somnologica-3TM (Medcare) software, each 4 s epoch of the EEG
573 signal was subjected to discrete Fourier transform to determine EEG power density (spectra 0–90 Hz
574 at a frequency resolution of 0.25 Hz). We used artifact-free, same-state–flanked 4 s epochs to calculate
575 the mean EEG spectral profiles for each behavioral states and time intervals. To account for differences
576 among animals in absolute EEG power, the mean values of spectral profiles were converted into
577 percentages relative to a baseline EEG power reference value of 100%. This reference value was
578 determined for each mouse by summing the power within the frequency range of 0.75–47.5 Hz across
579 all states and throughout the first day of baseline recordings. To control for differences in the amount
580 of wakefulness, NREMS and REMS, this reference was weighted so that the relative contribution of
581 each state was identical for all mice (77). Time-frequency heatmaps of EEG power during wakefulness
582 were generated using methods described previously (78).
583
584 **Time-course analysis.** To examine the dynamic changes of EEG power within specific frequency
585 ranges throughout the day and night, the time-course of the activity of that frequency band was
586 computed for 4 s epochs scored as state of interest (NREMS, REMS and wake). For this purpose, the
587 epochs for each state were divided into percentiles, ensuring that each percentile contained a roughly
588 equal number of epochs. The number of percentiles for NREMS and REMS were: 12 for light periods,
589 6 for dark periods, and 8 for the 6-h light period after SD; for waking state: 6 for light periods, 12 for
590 dark periods, 8 for the 6-h light SD, and 4 for the 6-h light after SD. The average EEG power within the
591 specified frequency range was computed for each percentile, and subsequently normalized based on
592 the type of analysis. This normalization was either done relative to the total power of the baseline state
593 or with respect to the power achieved within the delta frequency band during slow-wave sleep at ZT8-
594 12. Like power density analysis, single epochs were excluded and only power values of the epochs that
595 themselves, as well as the two adjacent ones, were scored as artifact-free same-state were included in
596 the analysis.
597
598 **Theta-gamma cross-frequency coupling.** We used the modulation index (MI) to measure the theta-
599 gamma phase-amplitude coupling (30, 79). Using finite impulse response filters with an order equal to
600 three cycles of the low cutoff frequency, we first bandpass-filtered EEG signals into theta (6-11 Hz) and
601 fast-gamma (54-90 Hz) in both forward and reverse directions to eliminate phase distortion. We then
602 estimated instantaneous phase of theta and the envelope of fast-gamma using the Hilbert transform.
603 Theta phase was discretized into 18 equal bins (N=18, each 20°) and the average value of fast-gamma
604 envelope within each bin was calculated. The resulting phase-amplitude histogram (P) was compared

605 with a uniform distribution (*U*) using the Kullback-Leibler distance, $D_{KL}(P,U) = \sum_{j=1}^{N} P(j) *$
606 $log[P(j)/U(j)]$, and normalized by *log(N)* to obtain the modulation index, *MI* = D_{KL} / *log(N)*. To explore
607 possible coupling patterns between different pairs of low and high frequency bands, we used the
608 comodulogram analysis (79). We considered 16 frequency bands for phase (1-18 Hz, 1-Hz increments,
609 2-Hz bandwidth), and 14 frequency bands for amplitude (15-90 Hz, 5-Hz increments, 10-Hz bandwidth).
610 MI values were then calculated for all these pairs to obtain the comodulogram graph.
611
612 **Detection of sleep spindles.** NREMS spindles were detected automatically using an optimized
613 wavelet-based method as previously described (29). Briefly, the power of EEG signals within 9-16Hz
614 was estimated using the complex B-spline wavelet function, and smoothed using a 200 ms Hanning
615 window, and then a threshold equal to 3 SD (SD: standard deviation) above the mean was applied to
616 detect the potential spindle events. Events shorter than 400 ms or longer than 2 s were discarded. Using
617 band pass-filtered EEG signals in the spindle range (9–16 Hz), we automatically counted the number
618 of cycles of each detected event and excluded those with <5 cycles or more than 30 cycles. To discard
619 artefacts, events with a power in the spindle band lower than 6–8.5 Hz or 16.5–20 Hz power bands
620 were not included.
621
622 **Statistical analysis.** The specific number (n) of replicates employed in each experiment is provided in
623 the corresponding figure legends. The individuals responsible for conducting SD and scoring the sleep
624 recordings were unaware of the genotype of the animals, ensuring blinding during these procedures.
625 The results are presented as mean ± SEM or mean ± SD. Statistical analyses were conducted using
626 GraphPad Prism. The significance of comparisons was determined using one- or two-way ANOVA or
627 mix effect model followed by relevant post hoc tests and are reported in the figure legends.
628
629
630
631
632

633 **Figure legends**

634 **Figure 1. Large transcriptional changes in the microglia and CAMs of WT and Ox-Ataxin**
635 **mice after SD** (**A**) (Left) Representative confocal image of parenchymal microglia (IBA1$^+$,
636 green) and perivascular (yellow arrowheads) and meningeal (white arrowheads) CAMs (IBA1$^+$
637 and CD206$^+$, red). (Right) CAMs are positive for CD206 protein expression and are found in
638 the collagen (Col) IV$^+$ perivascular and meningeal compartment. (**B**) Microglia were sorted as
639 CD11b$^+$; CD45^{Intermediate} populations, separately from the cortex and hypothalamus of WT and
640 Ox-Ataxin-Tg mice. CAMs were sorted as CD11b$^+$ and CD206$^+$ populations from the whole
641 brain of both genotypes. (**C**) Heatmap representation showing differentially expressed genes
642 in microglia from hypothalamus and cortex of WT mice under SD or control conditions. Each
643 column represents microglial gene expression from one individual mouse, with 4-5 mice per
644 group. Linear color scale. (**D**) Gene set enrichment analysis for DEGs in microglia of WT mice.
645 (**E**) Heatmaps depicting DEGs in CAMs of WT mice under SD or control conditions. Each
646 column represents CAM gene expression from one individual mouse, with 4-5 mice per group.
647 Linear color scale. (**F**) Bar plots depicting *App* and *Lyve-1* gene expression under SD or control
648 conditions in CAMs of WT mice. Values are mean ± SEM, n=4-5 (t-test, *P < 0.05; **P < 0.01;
649 ***P < 0.001). (**G**) Gene set enrichment analysis for DEGs in CAMs of WT mice. (**H**) Heatmaps
650 depicting DEGs in microglia from hypothalamus and cortex of Ox-Ataxin mice under SD or
651 control conditions. (**I**) Venn diagram depicting the numbers of differentially regulated and
652 overlapping genes between microglia of WT and OX-Ataxin mice. Red and blue represent up-
653 and down-regulated genes, respectively. (**J**) Gene set enrichment analysis for DEGs in
654 microglia of Ox-Ataxin mice. (**K**, **L**, **M** and **N**) Radar plots representing DEGs in microglia of
655 cortex (Cx) and hypothalamus (Hy) in WT (green dots) and Ox-Ataxin (blue dots) mice under
656 SD (white, top) or control (noSD) condition (yellow, bottom). (**O**) Heatmaps depicting DEGs
657 between the SD and control groups in CAMs of Ox-Ataxin mice. Each column represents CAM
658 gene expression from one individual mouse, with 4-5 mice per group. Linear color scale. The
659 number of DEGs in response to sleep loss in CAMs of Ox-Ataxin mice is markedly diminished
660 relative to WT mice

661

662 **Figure 2. Essential role of MG in regulation of NREMS and associated EEG oscillations.**
663 (**A**) Schematic illustration of the experimental procedure conducted on adult mice to assess
664 the brain's electrical activity using EEG. Recordings prior to PLX5622 drug administration
665 served as controls. Mice were then fed PLX5622-containing food during 2 weeks. During the
666 final 3 days of this 2-week period, a 2nd series of recordings was conducted. Following
667 PLX5622 treatment, mice were provided control food for 4 weeks. After 4 weeks under normal
668 food, a 3rd recording was performed. All 3 recordings were performed on the same mice. (**B,**
669 **C**) PLX5622 substantially depleted the microglia from the brain within 2 weeks (compare
670 control and MG-Dep). Return to normal food repopulated microglia into the brain after 4 weeks
671 (compare MG-Dep and MG-Repop). (**D**) Recording paradigm. The first 2 days of recordings
672 served as baseline, averaged as one day. The 2nd day consisted of 6 h SD followed by 18 h
673 of recovery. (**E**) Time-course of vigilance states; Wakefulness (top) and NREMS (bottom).
674 Compared to controls (black datapoints), MG-Dep (orange datapoints) and –Repop (blue
675 datapoints) mice show a large increase in NREMS duration during the dark period both at
676 baseline and during recovery (n = 9 for control and MG-Depleted conditions and n = 6 for MG-
677 Repopulated condition, 2-way ANOVA, followed by Dunnett's test, *P < 0.05; **P < 0.01; ***P
678 < 0.001, orange and blue stars, significant differences between control and MG-Dep and MG-
679 Repop mice, respectively). Data points are shown in minutes per hour (min/h) and represent
680 the average of 2 h. (**F**) From left to right: Time in wakefulness (top) and NREMS (bottom)
681 during baseline light, dark and recovery light and dark periods (Mixed-effects analysis,
682 followed by Dunnett's test, *P < 0.05; **P < 0.01; ***P < 0.001). (**G**) Time-course of EEG delta
683 power (1–4 Hz) during the 3-day recording. EEG delta power is a proxy of sleep need. Both
684 MG-Dep and MG-Repop mice show deficiency in building up sleep need during the dark period
685 (2-way ANOVA, followed by Dunnett's test, *P < 0.05; **P < 0.01; ***P < 0.001, orange and
686 blue stars, significant differences between control and MG-Dep and MG-Repop mice,
687 respectively). (**H**) EEG power spectra of experimental mice in NREMS during baseline light
688 (left) and dark (right) periods. EEG power is expressed as % of baseline power of control
689 condition. Insets show amplification of specific EEG frequencies (2-way ANOVA, followed by
690 Dunnett's test, *P < 0.05; **P < 0.01; ***P < 0.001, orange and blue stars indicate significant
691 differences between control and MG-Depleted and MG-Repopulated mice, respectively). (**I**)
692 EEG power spectra of experimental mice in NREMS during recovery light (left) and dark (right)
693 periods. (**J**) Distribution of NREMS bout durations during baseline dark period across the
694 experimental mice. Sleep bout duration is represented on the x-axis (1-way ANOVA, followed
695 by Tukey test). (**K**) (Top) Representative time-frequency heatmap of spindles. (Bottom)
696 Representative EEG/EMG signals of a detected spindle. Dashed horizontal lines indicate
697 upper and lower thresholds used to detect spindles with wavelet energy within 9-16 Hz, and

698 dashed vertical lines indicate the start and end of the detected spindle. (**L**) Spindle rate during
699 NREMS episodes in different conditions. Spindle rate significantly decreased in MG-depleted
700 mice (mixed-effects analysis, followed by Dunnett's test, *P < 0.05; **P < 0.01; ***P < 0.001)).
701
702 **Figure 3. REMS regulation largely depends on the presence of the MG.** (**A**) Time-course
703 of REMS duration in control (black), MG-Dep (orange) and MG-Repop (blue) mouse groups.
704 MG-Dep mice exhibit a large increase in REMS time during the baseline dark period (n = 9 for
705 control and MG-Dep conditions and n = 6 for MG-Repop condition, 2-way ANOVA, followed
706 by Dunnett's test, *P < 0.05; **P < 0.01; ***P < 0.001, orange and blue stars represent
707 significant differences between control and MG-Dep and MG-Repop mice, respectively). Data
708 points are shown in minutes per hour (min/h) and represent the average of 2 h. (**B**) Time in
709 REMS during baseline dark period (mixed-effects analysis, followed by Dunnett's test, *P <
710 0.05; **P < 0.01; ***P < 0.001). (**C**) Distribution of REMs bout durations during baseline dark
711 period across 3 mouse groups. Sleep bout duration is presented as x-axis (1-way ANOVA,
712 followed by Tukey test). (**D**) EEG power spectra of all experimental mice in REMS during
713 baseline dark period. Insets show amplification for specific EEG frequencies (2-way ANOVA,
714 followed by Dunnett's test, *P < 0.05; **P < 0.01; ***P < 0.001, orange and blue stars are
715 significant differences between control mice and MG-Dep and MG-Repop mice respectively).
716 (**E**) Comodulogram graphs show the modulation index for a wide range of frequency pairs,
717 obtained from 12-h recordings of one animal in different conditions. (**F**) Normalized theta-
718 gamma coupling across 3 experimental conditions. Theta-gamma coupling is significantly
719 decreased in MG-depleted and -repopulated conditions (mixed-effects analysis, followed by
720 Dunnett's test, *P < 0.05; **P < 0.01; ***P < 0.001)).
721 .
722
723 **Figure 4. MG Repopulation fails to normalize the waking state deficits induced by MG**
724 **depletion.** (**A**) Time x frequency x power heatmap representations of the waking EEG of
725 control, MG-Dep and MG-Repop mice across the 3 recorded days (48 h baseline, 6 h sleep
726 deprivation and 18 h recovery) show large changes in higher frequency bands. (**B**) EEG power
727 spectra of experimental mice in wakefulness during baseline light and dark periods (2-way
728 ANOVA, followed by Dunnett's test, *P < 0.05; **P < 0.01; ***P < 0.001, orange star are
729 significant differences between control mice and MG-Dep mice). (**C**) Time-course of TDW
730 amounts indicates decreased TDW time during the dark period in MG-Dep and MG-Rep.
731 Datapoints are shown in min/h and represent the average of 2 h (baseline days 1 and 2 are
732 averaged), (2-way ANOVA followed by Dunnett's test, orange and blue stars are significant
733 differences between control and MG-Dep and MG-Repop mice, respectively). (**D**)
734 Quantification of time in TDW (min/h) during baseline light and dark period (mixed-effects

735 analysis, followed by Dunnett's test, *P < 0.05; **P < 0.01; ***P < 0.001). (**E**) Time in TDW
736 during SD. (**F**) Waking EEG slow-gamma (32-45 Hz) power dynamics during the 3-day
737 recording (baseline days 1 and 2 are averaged) (2-way ANOVA, followed by Dunnett's test).
738
739 **Figure 5. Large synaptic imbalance after MG depletion and repopulation.** (**A**) Schematic
740 illustration of the cell types for which the number of synapses was counted. NEUN (blue) and
741 PV (orange) positive neurons in the cortex and HCRT neurons in the hypothalamus. The
742 number of co-localized excitatory VGLUT1-HOMER1 synaptic proteins on NEUN, PV and
743 HCRT positive neurons were counted. Additionally, the number of co-localized inhibitory
744 SYT2-Gephyrin synaptic proteins on NEUN neurons were counted. (**B**) Representative image
745 depicting pre, postsynaptic proteins and their colocalization in a NEUN positive neuron.
746 Synapses (arrowheads) are marked with pink color using ImageJ macro (right). Scale bar:
747 10μm. (**C**) Number of VGLUT1-HOMER1 synapses/μm^2 of $NEUN^+$ soma. N=342 cells from
748 12 mice for control, 324 cells from 11 mice for MG-Dep, and 357 cells from 12 mice for MG-
749 Repop conditions. The data show a reduced number of these synapses in both MG-Dep and
750 MG-Repop conditions (**D**) Number of HOMER1 puncta/μm^2 of $NEUN^+$ soma. (**E**) Number of
751 VGLUT1 puncta/μm^2 of NEUN+ soma. (**F**) Number of SYT2-Gephyrin synapses/μm^2 of
752 $NEUN^+$ soma. N=299 cells from 12 mice for control, 270 cells from 11 mice for MG-Dep, and
753 306 cells from 12 mice for MG-Repop conditions. (**G**) Representative images depicting SYT2-
754 Gephyrin synapses in $NEUN^+$ cortical neuron. Large increase in these inhibitory synapses is
755 observed in the MG-Repop condition. Scale bar: 10 μm. (**H**) Distribution of PV^+ neurons (red)
756 in the cortex. Scale bar: 100 μm (left), 10 μm (right). (**I**) Number of vGLUT1-HOMER1
757 synapses/μm^2 of PV^+ soma. N=29 cells from 5 mice for control, 29 cells from 5 mice for MG-
758 Dep, and 23 cells from 4 mice for MG-Repop conditions. (**J**) Left, distribution of $HCRT^+$
759 neurons (red) in the lateral hypothalamus. Right, a $HCRT^+$ neuron stained with VGLUT1
760 (green) and HOMER1 (Cyan). Scale bar: 100 and 10 μm. (**K**) Number of VGLUT1-HOMER1
761 synapses/μm^2 of HCRT+ soma. N=70 cells from 3 mice for control, 73 cells from 3 mice for
762 MG-Dep, and 77 cells from 4 mice for MG-Repop conditions. (**L**) Gene expression of synaptic
763 proteins and neurotransmitter receptors at RNA level following MG depletion and repopulation.
764 N=3 for control and MG-Dep and n=4 for MG-Repop conditions. 1-way ANOVA, followed by
765 Tukey test, *P < 0.05; **P < 0.01; ***P < 0.001.
766
767 **Figure 6. MG repopulation largely restores the metabolite changes induced by**
768 **microglial depletion.** (**A**) PCA of targeted metabolites in cortex isolated from control (n=3),
769 MG depleted (n=3) and repopulated (n=4) mice. (**B**) LC-MS/MS assessment of the
770 neurotransmitter content in the brain of control, MG-Dep and MG-Repop mice. (**C**)

771 Downregulation of amino acids in the brain of experimental mice after MG depletion. 1-way
772 ANOVA, followed by Tukey test, *P < 0.05; **P < 0.01; ***P < 0.001.
773
774
775 **Figure S1: Transcriptional changes in microglial core genes following sleep**
776 **deprivation.** (**A**) Bar plots showing the expression of microglial core genes in the cortex and
777 hypothalamus under SD and NoSD (control) conditions. The color codes are provided. (**B**) Bar
778 plots showing the expression of the *Adrb2* gene. *P < 0.05; **P < 0.01; ***P < 0.001.

779 **Figure S2: Region and genotype specific transcriptional changes in microglial genes**
780 **following sleep deprivation.**

781 Heatmap showing differentially expressed genes in microglia of the cortex and hypothalamus
782 in WT and Ox-Ataxin mice under SD and control conditions. Each column represents microglia
783 data from one individual mouse, with 4-5 mice per group. The color code represents a linear
784 scale.

785

References

1. K. Ramar *et al.*, Sleep is essential to health: an American Academy of Sleep Medicine position statement. *J Clin Sleep Med* 10.5664/jcsm.9476 (2021).
2. A. A. Borbély, A two process model of sleep regulation. *Hum Neurobiol* **1**, 195-204 (1982).
3. G. F. Gilestro, G. Tononi, C. Cirelli, Widespread changes in synaptic markers as a function of sleep and wakefulness in Drosophila. *Science* **324**, 109-112 (2009).
4. S. Maret *et al.*, Homer1a is a core brain molecular correlate of sleep loss. *Proc Natl Acad Sci U S A* **104**, 20090-20095 (2007).
5. C. B. Saper, T. C. Chou, T. E. Scammell, The sleep switch: hypothalamic control of sleep and wakefulness. *Trends Neurosci* **24**, 726-731 (2001).
6. L. Amann, T. Masuda, M. Prinz, Mechanisms of myeloid cell entry to the healthy and diseased central nervous system. *Nat Immunol* **24**, 393-407 (2023).
7. K. Kierdorf, T. Masuda, M. J. C. Jordão, M. Prinz, Macrophages at CNS interfaces: ontogeny and function in health and disease. *Nat Rev Neurosci* **20**, 547-562 (2019).
8. M. Prinz, T. Masuda, M. A. Wheeler, F. J. Quintana, Microglia and Central Nervous System-Associated Macrophages-From Origin to Disease Modulation. *Annual review of immunology* **39**, 251-277 (2021).
9. M. Prinz, S. Jung, J. Priller, Microglia Biology: One Century of Evolving Concepts. *Cell* **179**, 292-311 (2019).
10. R. C. Paolicelli *et al.*, Synaptic pruning by microglia is necessary for normal brain development. *Science (New York, N.Y.)* **333**, 1456-1458 (2011).
11. K. Kierdorf *et al.*, Microglia emerge from erythromyeloid precursors via Pu.1- and Irf8-dependent pathways. *Nature neuroscience* **16**, 273-280 (2013).
12. C. Schulz *et al.*, A lineage of myeloid cells independent of Myb and hematopoietic stem cells. *Science (New York, N.Y.)* **336**, 86-90 (2012).
13. J. Bruttger *et al.*, Genetic Cell Ablation Reveals Clusters of Local Self-Renewing Microglia in the Mammalian Central Nervous System. *Immunity* **43**, 92-106 (2015).
14. T. L. Tay *et al.*, A new fate mapping system reveals context-dependent random or clonal expansion of microglia. *Nature neuroscience* **20**, 793-803 (2017).
15. Y. Huang *et al.*, Repopulated microglia are solely derived from the proliferation of residual microglia after acute depletion. *Nat Neurosci* **21**, 530-540 (2018).
16. M. J. Pinto *et al.*, Microglial TNFα orchestrates protein phosphorylation in the cortex during the sleep period and controls homeostatic sleep. *Embo j* **42**, e111485 (2023).
17. M. E. Choudhury *et al.*, Phagocytic elimination of synapses by microglia during sleep. *Glia* **68**, 44-59 (2020).
18. G. Corsi *et al.*, Microglia modulate hippocampal synaptic transmission and sleep duration along the light/dark cycle. *Glia* **70**, 89-105 (2022).
19. A. M. Ingiosi, M. R. Opp, J. M. Krueger, Sleep and immune function: glial contributions and consequences of aging. *Current opinion in neurobiology* **23**, 806-811 (2013).
20. L. H. Tuan, L. J. Lee, Microglia-mediated synaptic pruning is impaired in sleep-deprived adolescent mice. *Neurobiol Dis* **130**, 104517 (2019).
21. M. Bellesi *et al.*, Sleep Loss Promotes Astrocytic Phagocytosis and Microglial Activation in Mouse Cerebral Cortex. *J Neurosci* **37**, 5263-5273 (2017).
22. A. Drieu *et al.*, Parenchymal border macrophages regulate the flow dynamics of the cerebrospinal fluid. *Nature* **611**, 585-593 (2022).
23. Y. W. Zhang, R. Thompson, H. Zhang, H. Xu, APP processing in Alzheimer's disease. *Mol Brain* **4**, 3 (2011).
24. J. Hara *et al.*, Genetic ablation of orexin neurons in mice results in narcolepsy, hypophagia, and obesity. *Neuron* **30**, 345-354 (2001).
25. A. Vassalli, P. Franken, Hypocretin (orexin) is critical in sustaining theta/gamma-rich waking behaviors that drive sleep need. *Proc Natl Acad Sci U S A* **114**, E5464-e5473 (2017).

26. N. N. Dagher *et al.*, Colony-stimulating factor 1 receptor inhibition prevents microglial plaque association and improves cognition in 3xTg-AD mice. *J Neuroinflammation* **12**, 139 (2015).
27. H. Van Hove *et al.*, A single-cell atlas of mouse brain macrophages reveals unique transcriptional identities shaped by ontogeny and tissue environment. *Nat Neurosci* **22**, 1021-1035 (2019).
28. A. Seifinejad, S. Li, M. L. Possovre, A. Vassalli, M. Tafti, Hypocretinergic interactions with the serotonergic system regulate REM sleep and cataplexy. *Nat Commun* **11**, 6034 (2020).
29. M. Bandarabadi *et al.*, A role for spindles in the onset of rapid eye movement sleep. *Nat Commun* **11**, 5247 (2020).
30. M. Bandarabadi *et al.*, Dynamic modulation of theta-gamma coupling during rapid eye movement sleep. *Sleep* **42**, 1-11 (2019).
31. T. Endo *et al.*, Selective REM sleep deprivation in humans: effects on sleep and sleep EEG. *Am J Physiol* **274**, R1186-1194 (1998).
32. G. Tononi, C. Cirelli, Sleep and synaptic homeostasis: a hypothesis. *Brain Res Bull* **62**, 143-150 (2003).
33. I. Hristovska *et al.*, Sleep decreases neuronal activity control of microglial dynamics in mice. *Nat Commun* **13**, 6273 (2022).
34. K. Kon *et al.*, Cortical parvalbumin neurons are responsible for homeostatic sleep rebound through CaMKII activation. *bioRxiv* 10.1101/2023.04.29.537929, 2023.2004.2029.537929 (2023).
35. B. Bouhours, E. Gjoni, O. Kochubey, R. Schneggenburger, Synaptotagmin2 (Syt2) Drives Fast Release Redundantly with Syt1 at the Output Synapses of Parvalbumin-Expressing Inhibitory Neurons. *J Neurosci* **37**, 4604-4617 (2017).
36. M. Bellesi *et al.*, Effects of sleep and wake on oligodendrocytes and their precursors. *The Journal of neuroscience : the official journal of the Society for Neuroscience* **33**, 14288-14300 (2013).
37. M. Bellesi, L. de Vivo, G. Tononi, C. Cirelli, Effects of sleep and wake on astrocytes: clues from molecular and ultrastructural studies. *BMC biology* **13**, 66 (2015).
38. S. Dujardin *et al.*, Tau molecular diversity contributes to clinical heterogeneity in Alzheimer's disease. *Nat Med* **26**, 1256-1263 (2020).
39. N. Naidoo, Cellular stress/the unfolded protein response: relevance to sleep and sleep disorders. *Sleep Med Rev* **13**, 195-204 (2009).
40. L. Rajendran, R. C. Paolicelli, Microglia-Mediated Synapse Loss in Alzheimer's Disease. *J Neurosci* **38**, 2911-2919 (2018).
41. J. H. Roh *et al.*, Potential role of orexin and sleep modulation in the pathogenesis of Alzheimer's disease. *The Journal of experimental medicine* **211**, 2487-2496 (2014).
42. A. Gabelle *et al.*, Reduced brain amyloid burden in elderly patients with narcolepsy type 1. *Ann Neurol* **85**, 74-83 (2019).
43. Y. L. Tan, Y. Yuan, L. Tian, Microglial regional heterogeneity and its role in the brain. *Mol Psychiatry* **25**, 351-367 (2020).
44. P. Ayata *et al.*, Epigenetic regulation of brain region-specific microglia clearance activity. *Nat Neurosci* **21**, 1049-1060 (2018).
45. S. R. Morairty *et al.*, A role for cortical nNOS/NK1 neurons in coupling homeostatic sleep drive to EEG slow wave activity. *Proc Natl Acad Sci U S A* **110**, 20272-20277 (2013).
46. C. Cirelli, R. Huber, A. Gopalakrishnan, T. L. Southard, G. Tononi, Locus ceruleus control of slow-wave homeostasis. *J Neurosci* **25**, 4503-4511 (2005).
47. E. F. Willis *et al.*, Repopulating Microglia Promote Brain Repair in an IL-6-Dependent Manner. *Cell* **180**, 833-846.e816 (2020).
48. Y. Zhang *et al.*, Repopulating retinal microglia restore endogenous organization and function under CX3CL1-CX3CR1 regulation. *Sci Adv* **4**, eaap8492 (2018).

49. E. Favuzzi *et al.*, GABA-receptive microglia selectively sculpt developing inhibitory circuits. *Cell* **184**, 4048-4063.e4032 (2021).
50. D. K. Wilton, L. Dissing-Olesen, B. Stevens, Neuron-Glia Signaling in Synapse Elimination. *Annu Rev Neurosci* **42**, 107-127 (2019).
51. A. Badimon *et al.*, Negative feedback control of neuronal activity by microglia. *Nature* **586**, 417-423 (2020).
52. M. C. C. Guillaumin *et al.*, Deficient synaptic neurotransmission results in a persistent sleep-like cortical activity across vigilance states in mice. *bioRxiv* 10.1101/2023.05.11.540034, 2023.2005.2011.540034 (2023).
53. A. Seifinejad, A. Vassalli, M. Tafti, Neurobiology of cataplexy. *Sleep Med Rev* **60**, 101546 (2021).
54. A. Osorio-Forero *et al.*, Noradrenergic circuit control of non-REM sleep substates. *Current biology : CB* **31**, 5009-5023.e5007 (2021).
55. C. Ma *et al.*, Microglia Regulate Sleep via Calcium-Dependent Modulation of Norepinephrine Transmission. *bioRxiv* 10.1101/2023.07.24.550176, 2023.2007.2024.550176 (2023).
56. C. Ma *et al.*, Microglia regulate sleep through calcium-dependent modulation of norepinephrine transmission. *Nat Neurosci* **27**, 249-258 (2024).
57. R. D. Stowell *et al.*, Noradrenergic signaling in the wakeful state inhibits microglial surveillance and synaptic plasticity in the mouse visual cortex. *Nat Neurosci* **22**, 1782-1792 (2019).
58. Y. U. Liu *et al.*, Neuronal network activity controls microglial process surveillance in awake mice via norepinephrine signaling. *Nat Neurosci* **22**, 1771-1781 (2019).
59. M. Maugard, P. A. Vigneron, J. P. Bolanos, G. Bonvento, l-Serine links metabolism with neurotransmission. *Prog Neurobiol* **197**, 101896 (2021).
60. K. Vávrová, A. Hrabálek, P. Dolezal, T. Holas, J. Zbytovská, L-Serine and glycine based ceramide analogues as transdermal permeation enhancers: polar head size and hydrogen bonding. *Bioorg Med Chem Lett* **13**, 2351-2353 (2003).
61. H. Liu *et al.*, Microglia modulate stable wakefulness via the thalamic reticular nucleus in mice. *Nat Commun* **12**, 4646 (2021).
62. T. Masuda *et al.*, Novel Hexb-based tools for studying microglia in the CNS. *Nat Immunol* **21**, 802-815 (2020).
63. T. Masuda *et al.*, Specification of CNS macrophage subsets occurs postnatally in defined niches. *Nature* **604**, 740-748 (2022).
64. F. Lei *et al.*, CSF1R inhibition by a small-molecule inhibitor is not microglia specific; affecting hematopoiesis and the function of macrophages. *Proc Natl Acad Sci U S A* **117**, 23336-23338 (2020).
65. C. Mezö *et al.*, Different effects of constitutive and induced microbiota modulation on microglia in a mouse model of Alzheimer's disease. *Acta neuropathologica communications* **8**, 119 (2020).
66. O. Mossad *et al.*, Gut microbiota drives age-related oxidative stress and mitochondrial damage in microglia via the metabolite N(6)-carboxymethyllysine. *Nature neuroscience* **25**, 295-305 (2022).
67. A. Dobin *et al.*, STAR: ultrafast universal RNA-seq aligner. *Bioinformatics* **29**, 15-21 (2013).
68. J. Harrow *et al.*, GENCODE: the reference human genome annotation for The ENCODE Project. *Genome Res* **22**, 1760-1774 (2012).
69. M. E. Ritchie *et al.*, limma powers differential expression analyses for RNA-sequencing and microarray studies. *Nucleic Acids Res* **43**, e47 (2015).
70. S. X. Ge, D. Jung, R. Yao, ShinyGO: a graphical gene-set enrichment tool for animals and plants. *Bioinformatics* **36**, 2628-2629 (2020).
71. E. Favuzzi *et al.*, GABA-receptive microglia selectively sculpt developing inhibitory circuits. *Cell* **184**, 5686 (2021).

939 72. S. Behringer *et al.*, Targeted Metabolic Profiling of Methionine Cycle Metabolites and Redox
940 Thiol Pools in Mammalian Plasma, Cells and Urine. *Metabolites* **9** (2019).
941 73. A. C. Bravo *et al.*, Analysis of S-Adenosylmethionine and S-Adenosylhomocysteine: Method
942 Optimisation and Profiling in Healthy Adults upon Short-Term Dietary Intervention.
943 *Metabolites* **12**, 373 (2022).
944 74. L. Hannibal *et al.*, Metabolic Profiling in Human Fibroblasts Enables Subtype Clustering in
945 Glycogen Storage Disease. *Front Endocrinol (Lausanne)* **11**, 579981 (2020).
946 75. J. P. Maier *et al.*, Inhibition of metabotropic glutamate receptor III facilitates sensitization to
947 alkylating chemotherapeutics in glioblastoma. *Cell Death Dis* **12**, 723 (2021).
948 76. L. Moritz, K. Klotz, S. C. Grunert, L. Hannibal, U. Spiekerkoetter, Metabolic phenotyping in
949 phenylketonuria reveals disease clustering independently of metabolic control. *Mol Genet*
950 *Metab* **138**, 107509 (2023).
951 77. P. Franken, A. Malafosse, M. Tafti, Genetic variation in EEG activity during sleep in inbred
952 mice. *Am J Physiol* **275**, R1127-1137 (1998).
953 78. S. Li, P. Franken, A. Vassalli, Bidirectional and context-dependent changes in theta and
954 gamma oscillatory brain activity in noradrenergic cell-specific Hypocretin/Orexin receptor 1-
955 KO mice. *Sci Rep* **8**, 15474 (2018).
956 79. A. B. Tort *et al.*, Dynamic cross-frequency couplings of local field potential oscillations in rat
957 striatum and hippocampus during performance of a T-maze task. *Proc Natl Acad Sci U S A*
958 **105**, 20517-20522 (2008).

959

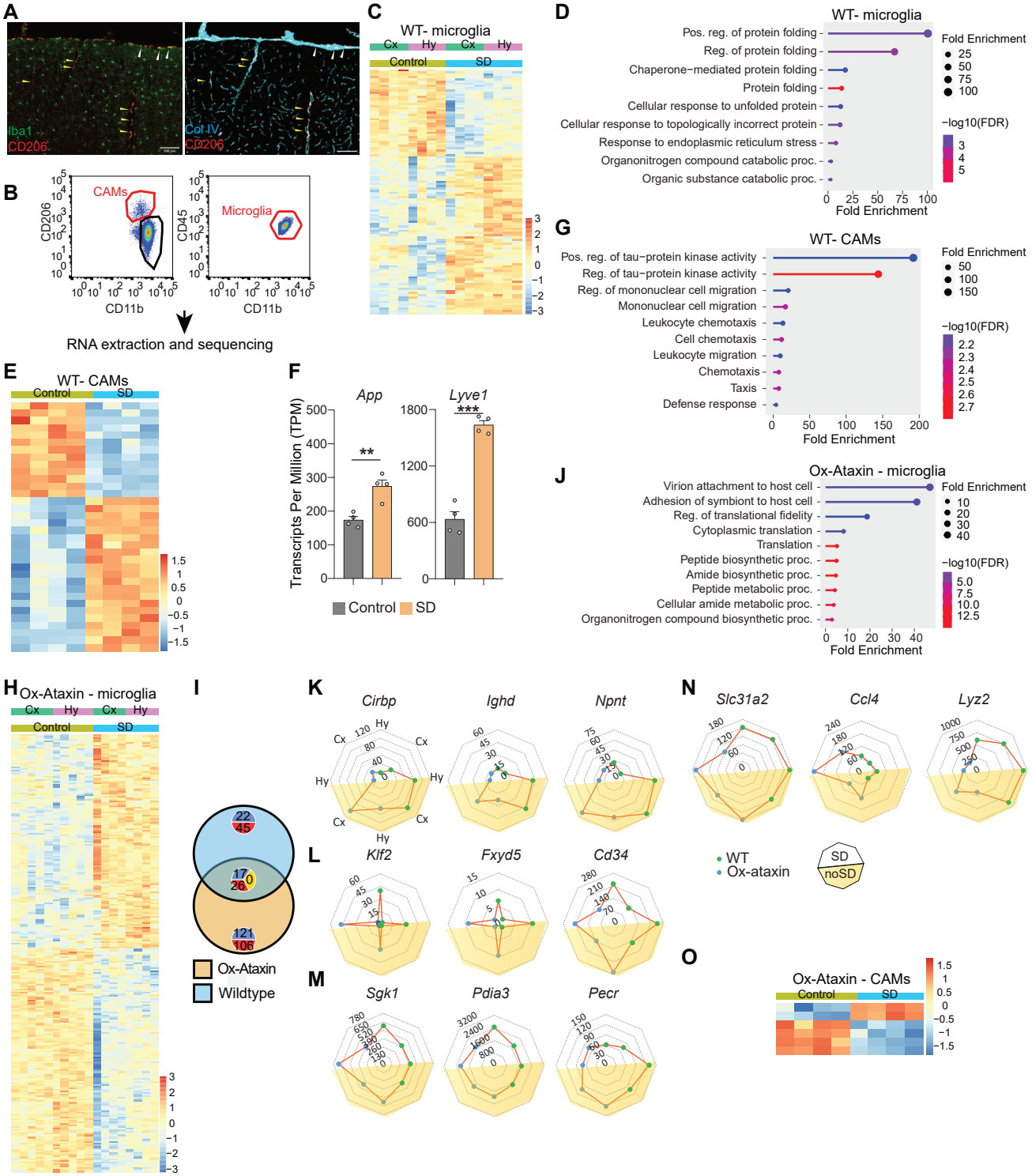
A
Iba1
CD206
Col IV
CD206
B
CAMs
Microglia
CD206
CD45
CD11b
CD11b
RNA extraction and sequencing
C
WT- microglia
Cx
Hy
Cx
Hy
Control
SD
D
WT- microglia
Pos. reg. of protein folding
Reg. of protein folding
Chaperone−mediated protein folding
Protein folding
Cellular response to unfolded protein
Cellular response to topologically incorrect protein
Response to endoplasmic reticulum stress
Organonitrogen compound catabolic proc.
Organic substance catabolic proc.
Fold Enrichment
−log10(FDR)
Fold Enrichment
E
WT- CAMs
Control
SD
F
App
Lyve1
Transcripts Per Million (TPM)
Control
SD
G
WT- CAMs
Pos. reg. of tau−protein kinase activity
Reg. of tau−protein kinase activity
Reg. of mononuclear cell migration
Mononuclear cell migration
Leukocyte chemotaxis
Cell chemotaxis
Leukocyte migration
Chemotaxis
Taxis
Defense response
Fold Enrichment
−log10(FDR)
Fold Enrichment
J
Ox-Ataxin - microglia
Virion attachment to host cell
Adhesion of symbiont to host cell
Reg. of translational fidelity
Cytoplasmic translation
Translation
Peptide biosynthetic proc.
Amide biosynthetic proc.
Peptide metabolic proc.
Cellular amide metabolic proc.
Organonitrogen compound biosynthetic proc.
Fold Enrichment
−log10(FDR)
Fold Enrichment
H
Ox-Ataxin - microglia
Cx
Hy
Cx
Hy
Control
SD
I
Ox-Ataxin
Wildtype
K
Cirbp
Ighd
Npnt
L
Klf2
Fxyd5
Cd34
M
Sgk1
Pdia3
Pecr
N
Slc31a2
Ccl4
Lyz2
WT
Ox-ataxin
SD
noSD
O
Ox-Ataxin - CAMs
Control
SD

Figure 1

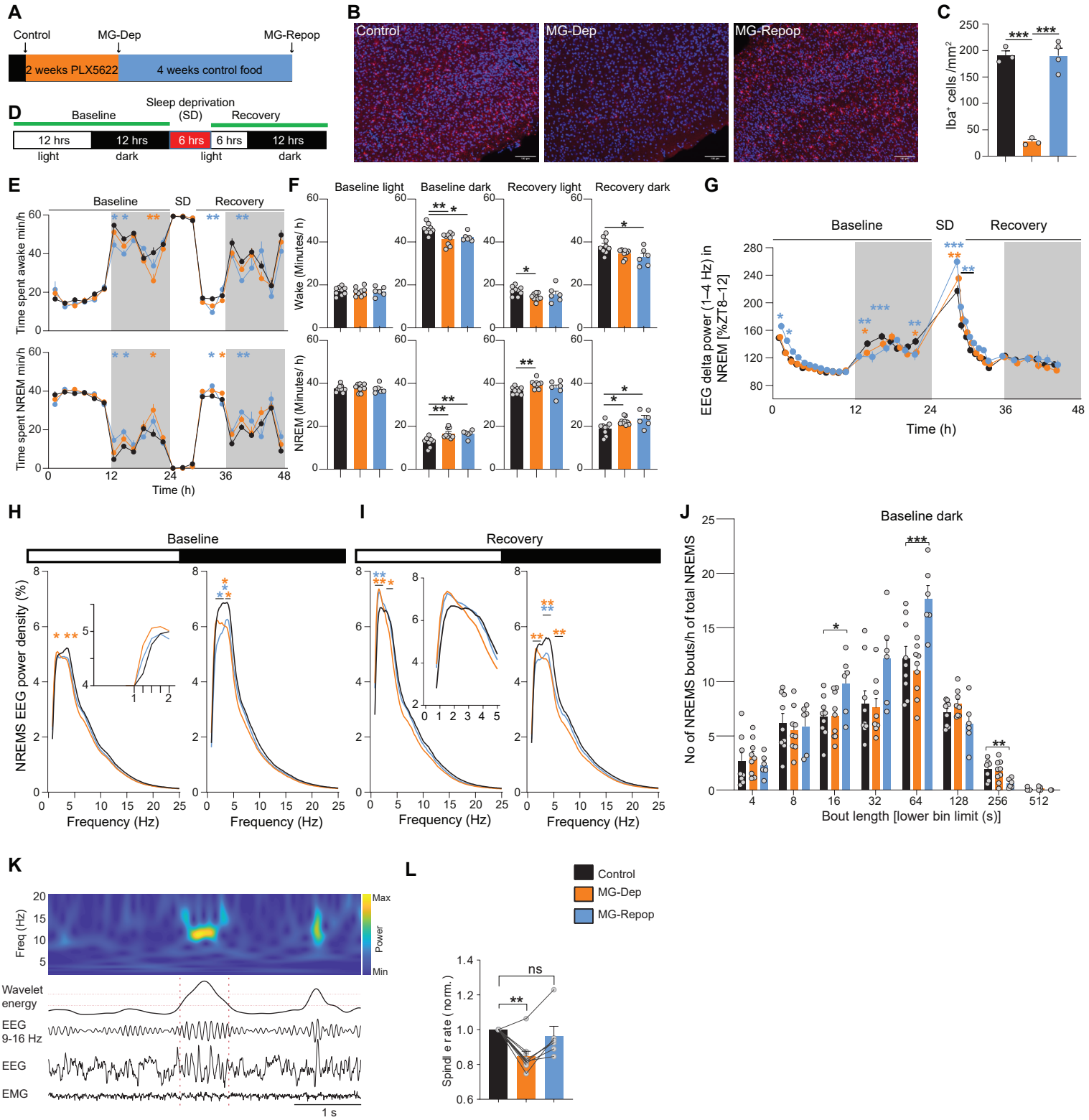
A
Control
MG-Dep
MG-Repop
2 weeks PLX5622
4 weeks control food
D
Baseline
Sleep deprivation (SD)
Recovery
12 hrs light
12 hrs dark
6 hrs light
6 hrs
12 hrs dark
B
Control
MG-Dep
MG-Repop
C
Iba+ cells /mm2
E
Baseline
SD
Recovery
Time spent awake min/h
Time spent NREM min/h
Time (h)
F
Baseline light
Baseline dark
Recovery light
Recovery dark
Wake (Minutes/ h)
NREM (Minutes/ h)
G
EEG delta power (1–4 Hz) in NREM [%ZT8–12]
Time (h)
H
Baseline
NREMS EEG power density (%)
Frequency (Hz)
I
Recovery
Frequency (Hz)
J
Baseline dark
No of NREMS bouts/h of total NREMS
Bout length [lower bin limit (s)]
K
Freq (Hz)
Max
Power
Min
Wavelet energy
EEG 9-16 Hz
EEG
EMG
1 s
L
Control
MG-Dep
MG-Repop
ns
Spindle rate (norm.)

Figure 2

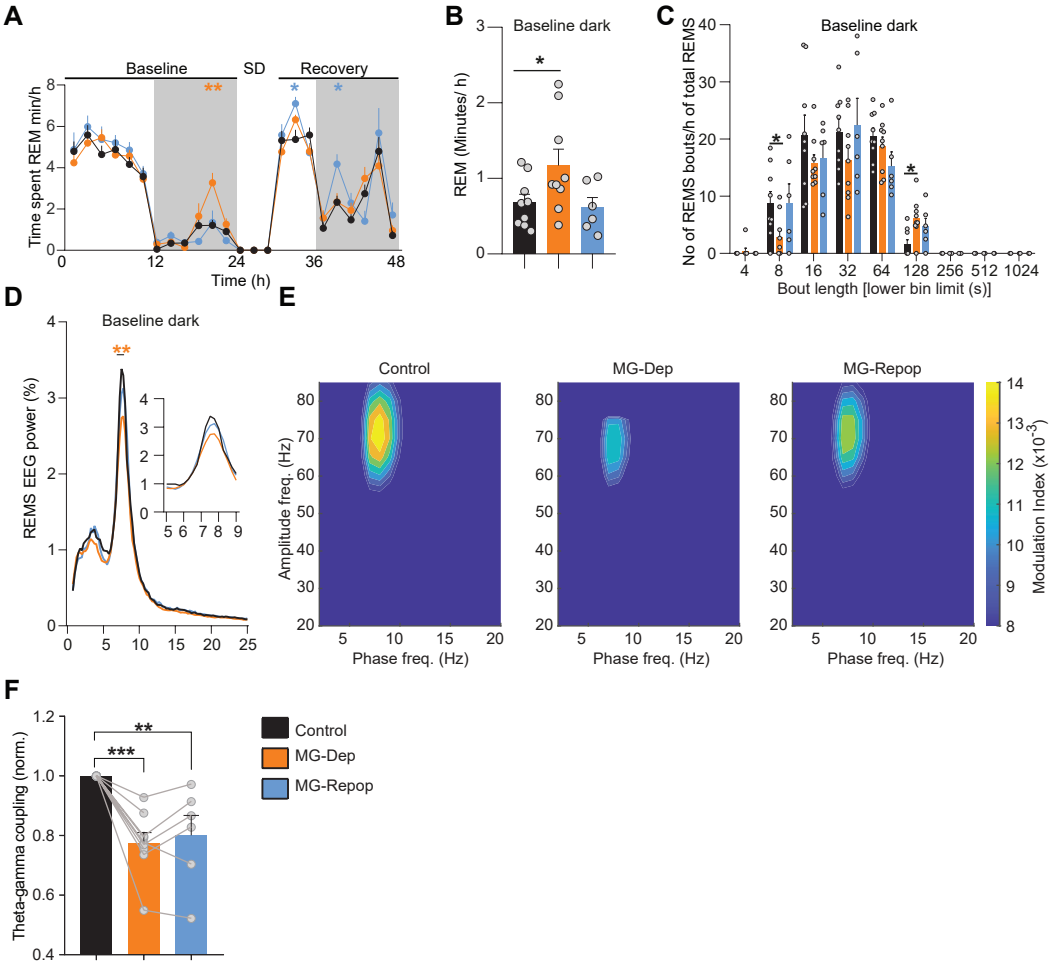
A
Baseline
SD
Recovery
Time spent REM min/h
Time (h)
B
Baseline dark
REM (Minutes/ h)
C
Baseline dark
No of REMS bouts/h of total REMS
Bout length [lower bin limit (s)]
D
Baseline dark
REMS EEG power (%)
E
Control
MG-Dep
MG-Repop
Amplitude freq. (Hz)
Phase freq. (Hz)
Modulation Index (x10-3)
F
Theta-gamma coupling (norm.)
Control
MG-Dep
MG-Repop

Figure 3

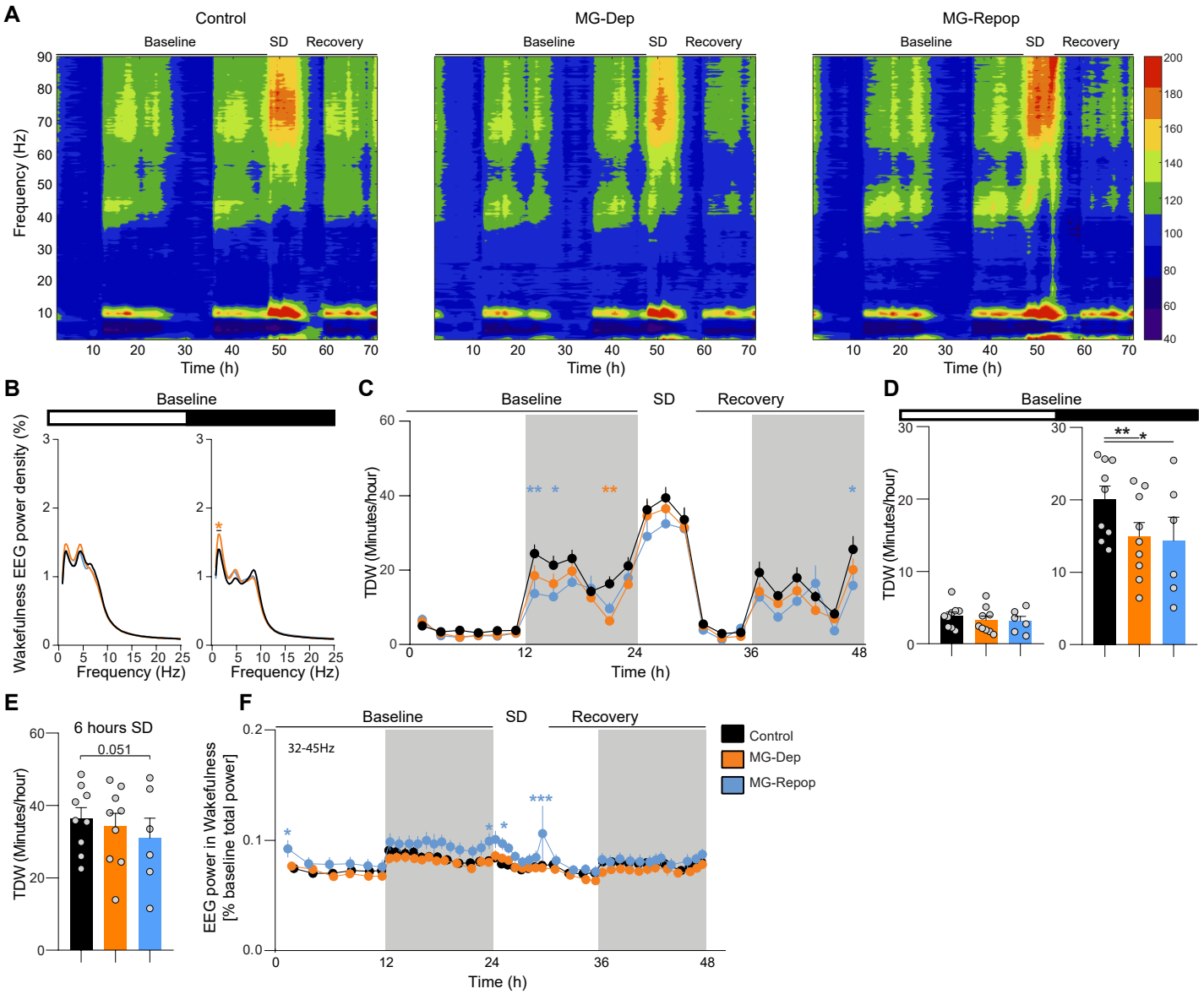
A
Control
MG-Dep
MG-Repop
Baseline
SD
Recovery
Frequency (Hz)
Time (h)
B
Wakefulness EEG power density (%)
Frequency (Hz)
C
TDW (Minutes/hour)
D
E
6 hours SD
0.051
F
32-45Hz
EEG power in Wakefulness [% baseline total power]
Control
MG-Dep
MG-Repop

Figure 4

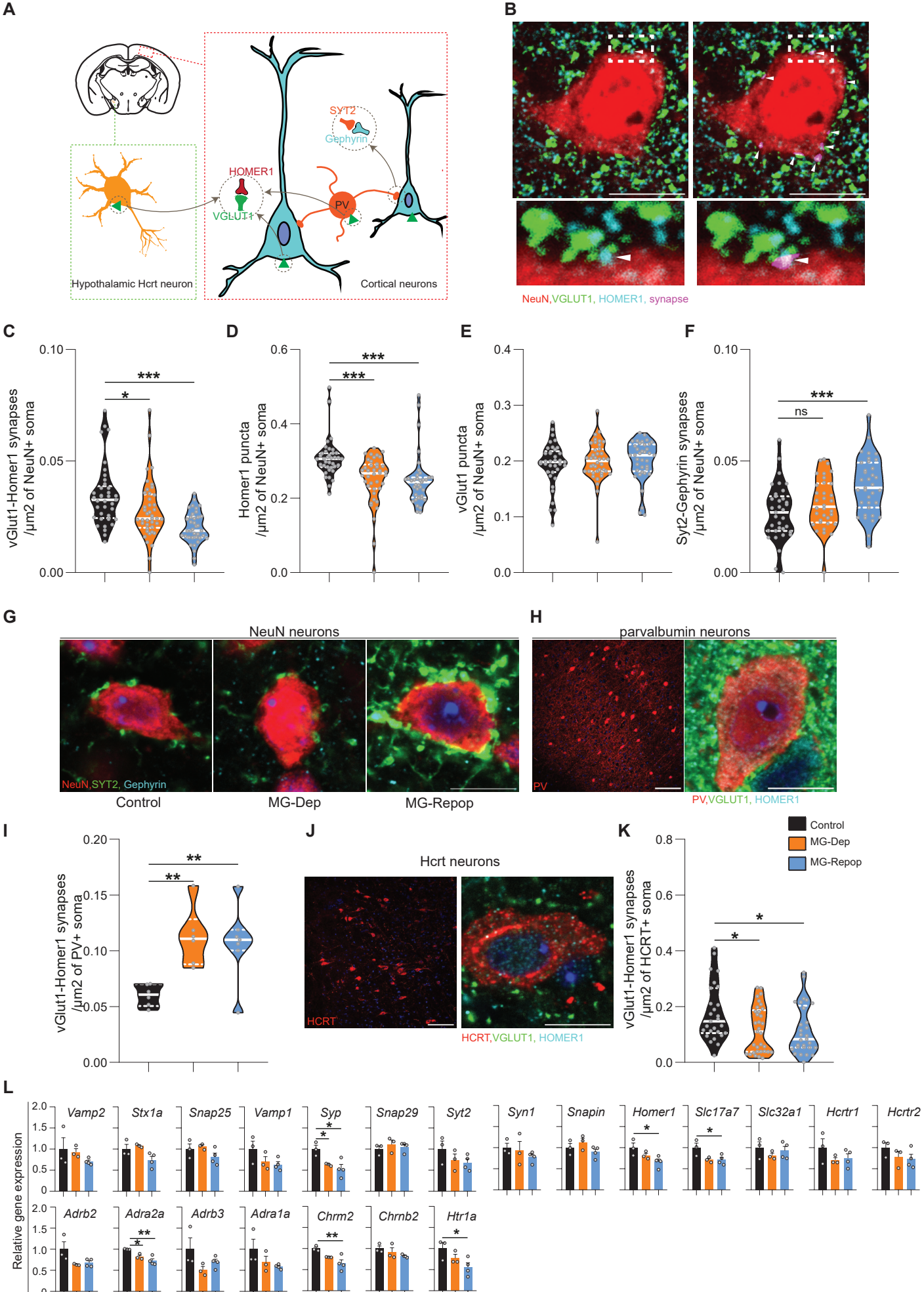
A
SYT2
Gephyrin
HOMER1
VGLUT1
PV
Hypothalamic Hcrt neuron
Cortical neurons
B
NeuN,VGLUT1, HOMER1, synapse
C
vGlut1-Homer1 synapses /µm2 of NeuN+ soma
D
Homer1 puncta /µm2 of NeuN+ soma
E
vGlut1 puncta /µm2 of NeuN+ soma
F
Syt2-Gephyrin synapses /µm2 of NeuN+ soma
ns
G
NeuN neurons
NeuN,SYT2, Gephyrin
Control
MG-Dep
MG-Repop
H
parvalbumin neurons
PV
PV,VGLUT1, HOMER1
I
vGlut1-Homer1 synapses /µm2 of PV+ soma
J
Hcrt neurons
HCRT
HCRT,VGLUT1, HOMER1
K
Control
MG-Dep
MG-Repop
vGlut1-Homer1 synapses /µm2 of HCRT+ soma
L
Relative gene expression
Vamp2
Stx1a
Snap25
Vamp1
Syp
Snap29
Syt2
Syn1
Snapin
Homer1
Slc17a7
Slc32a1
Hcrtr1
Hcrtr2
Adrb2
Adra2a
Adrb3
Adra1a
Chrm2
Chrnb2
Htr1a

Figure 5

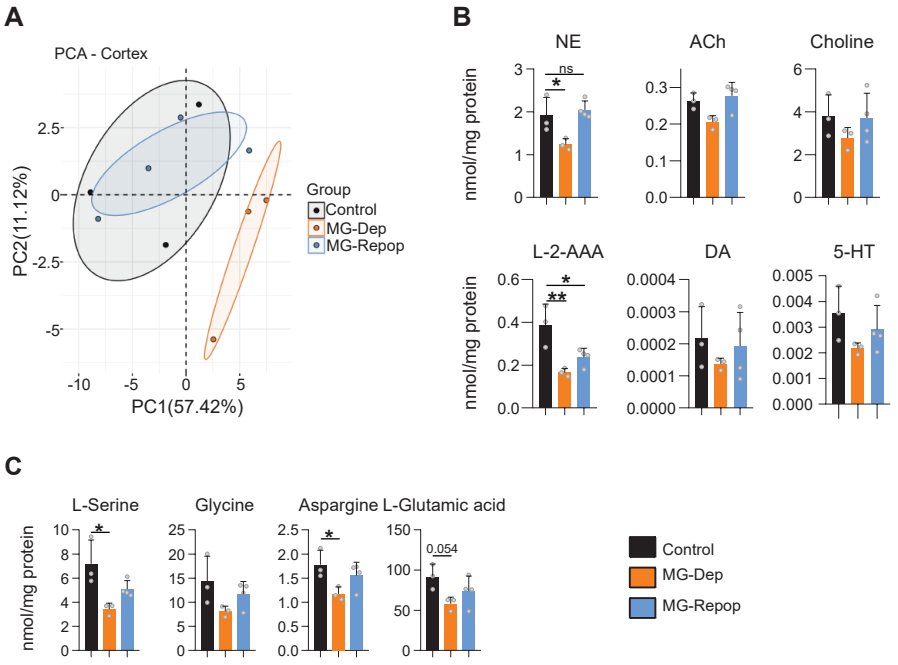
A
PCA - Cortex
PC2(11.12%)
PC1(57.42%)
Group
Control
MG-Dep
MG-Repop
B
NE
ACh
Choline
L-2-AAA
DA
5-HT
nmol/mg protein
ns
*
**
C
L-Serine
Glycine
Aspargine
L-Glutamic acid
0.054
Control
MG-Dep
MG-Repop

Figure 6

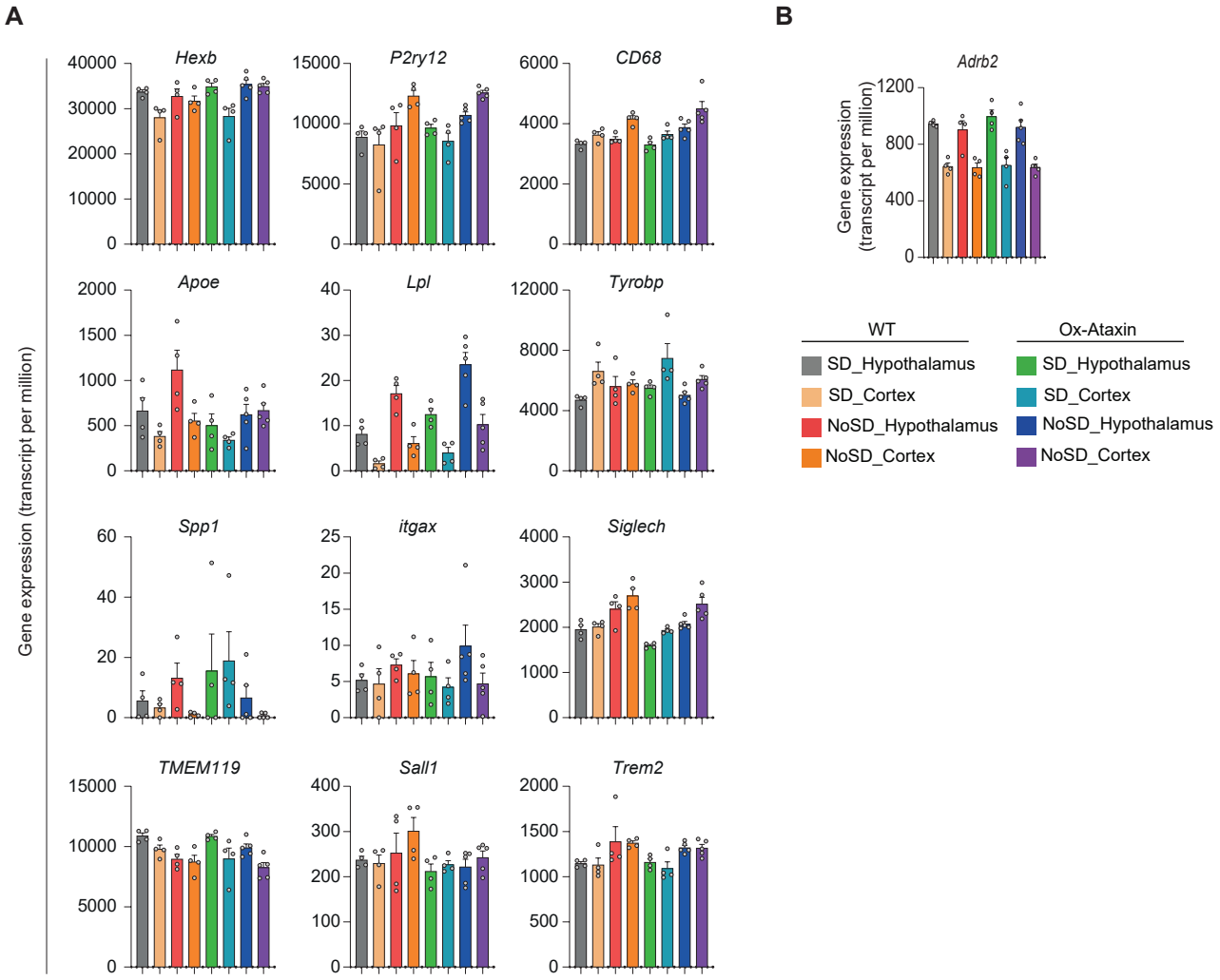
A
B
Gene expression (transcript per million)
Hexb
P2ry12
CD68
Apoe
Lpl
Tyrobp
Spp1
itgax
Siglech
TMEM119
Sall1
Trem2
Adrb2
WT
Ox-Ataxin
SD_Hypothalamus
SD_Cortex
NoSD_Hypothalamus
NoSD_Cortex

Figure S1

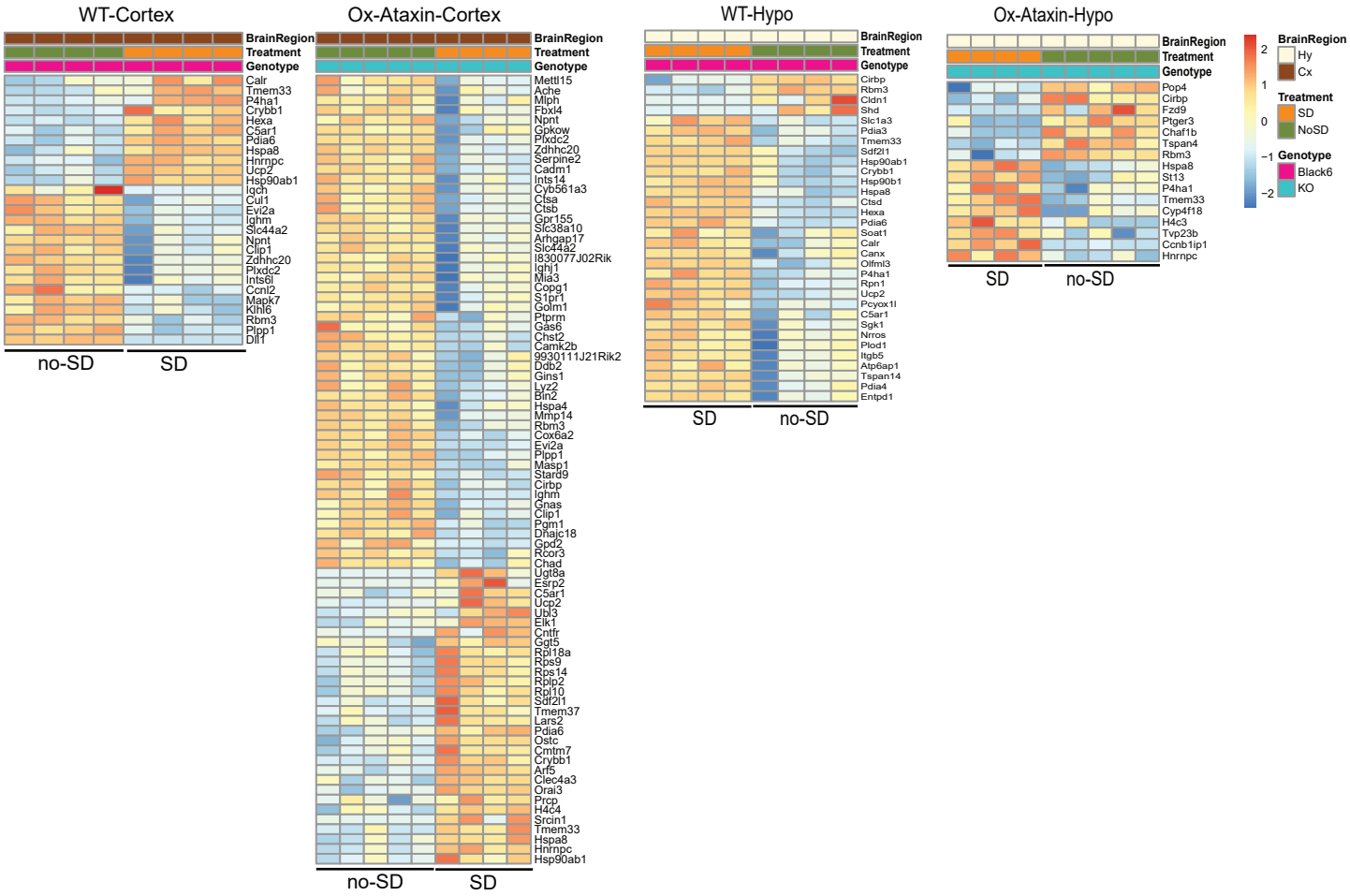
WT-Cortex
Ox-Ataxin-Cortex
WT-Hypo
Ox-Ataxin-Hypo
BrainRegion
Treatment
Genotype
no-SD
SD
Hy
Cx
NoSD
Black6
KO

Figure S2